

# Airborne Co-polarization and Cross-Polarization Observations of the Ocean-Surface NRCS at C-Band

Joseph W. Sapp, *Member, IEEE*, Suleiman O. Alsheiss, *Member, IEEE*, Zorana Jelenak, *Member, IEEE*, Paul S. Chang, *Member, IEEE*, Stephen J. Frasier, *Senior Member, IEEE*, and James Carswell, *Member, IEEE*

**Abstract**—Airborne co-polarization and cross-polarization observations of ocean surface normalized radar cross section (NRCS) were conducted over the North Atlantic during January and February 2015. Observations were made using the University of Massachusetts' Imaging Wind and Rain Airborne Profiler (IWRAP) radar system and a prototype antenna for the next-generation European scatterometer aboard MetOp-SG. Both were installed on a National Oceanic and Atmospheric Administration (NOAA) WP-3D research aircraft to characterize the wind response of the ocean-surface cross-polarization NRCS. During the flights, numerous constant-roll-angle circle maneuvers were performed at several different angles to collect NRCS measurements over a range of incidence angles. Surface winds at speeds between 8 and 34  $\text{ms}^{-1}$  were observed at incidence angles from 20° to 60° at all polarization combinations. The majority of measurements fell between 8 and 20  $\text{ms}^{-1}$ . Wind-direction dependence similar to copolarized NRCS was observed in the cross-polarized (VH) NRCS. The amplitude of the VH NRCS with respect to direction is less than that of copolarized NRCS at all wind speeds. Incidence angle dependence was also observed in the VH NRCS at all wind speeds. As a function of wind speed, the mean VH NRCS ( $A_0$ ) has a similar shape to the VV NRCS. The VH NRCS appears to not saturate at most incidence angles, unlike the VV and HH NRCS. VH and HH geophysical model functions (GMFs) were developed as functions of wind speed, incidence angle, and wind-relative azimuth for the wind speeds and incidence angles observed.

**Index Terms**—Airborne radar, C-band, cross-polarization, ocean vector winds, radar cross section, scatterometry.

## I. INTRODUCTION

SATELLITE-borne observations of sea-surface normalized radar cross section (NRCS) are routinely used to estimate ocean-surface vector winds. Scatterometers have traditionally used copolarized NRCS measurements for these retrievals. For example, the Advanced Scatterometers (ASCATs) currently operating aboard the European MetOp-1 and MetOp-2

Manuscript received November 4, 2015; revised March 10, 2016 and April 14, 2016; accepted May 23, 2016. Date of publication July 7, 2016; date of current version August 11, 2016. This work was supported by the National Oceanic and Atmospheric Administration Ocean Winds Program.

J. W. Sapp and S. O. Alsheiss are with Global Science and Technology, Inc., Greenbelt, MD 20740 USA, and also with NOAA/NESDIS Center for Satellite Applications Research (STAR), College Park, MD 20740 USA (e-mail: Joe.Sapp@noaa.gov).

Z. Jelenak and P. S. Chang are with NOAA/NESDIS Center for Satellite Applications (STAR), College Park, MD 20740 USA.

S. J. Frasier is with the Microwave Remote Sensing Laboratory, University of Massachusetts Amherst, Amherst, MA 01003 USA.

J. Carswell is with Remote Sensing Solutions, Inc., Barnstable, MA 02630 USA.

Color versions of one or more of the figures in this paper are available online at <http://ieeexplore.ieee.org>.

Digital Object Identifier 10.1109/TGRS.2016.2578048

satellites retrieve ocean-surface vector winds using C-band vertical polarization on transmit and receive (VV). This technique works well for low to moderate ocean-surface wind speeds; however, the sensitivity of copolarized NRCS at high wind speeds has been shown to decrease or even saturate [1]. More recently, studies using the C-band RADARSAT-2 synthetic aperture radar (SAR) instrument suggest that the cross-polarized (i.e., VH or HV) radar backscatter may not saturate at high wind speeds [2]–[4]. Other recent and more theoretical studies suggest that if there is signal saturation, it occurs at wind speeds higher than the copolarized saturation wind speeds [5], [6].

During January and February of 2015, the Ocean Winds Science Team at the NOAA Center for Satellite Applications and Research (STAR) performed a series of flight experiments over the North Atlantic Ocean with the NOAA WP-3D N42RF. Using the Imaging Wind and Rain Airborne Profiler (IWRAP), developed and maintained by the University of Massachusetts Amherst (UMass), in conjunction with an antenna on loan from the European Space Agency (ESA), experiments were designed to sample the cross-polarized ocean-surface NRCS at various wind speeds, azimuth angles with respect to wind direction, and incidence angles. This experiment campaign did not encounter winds stronger than marginal hurricane-force winds; therefore, the study presented here examines the moderate-speed behavior. Although some observations occurred above 30  $\text{ms}^{-1}$ , the majority fell between 8 and 20  $\text{ms}^{-1}$ .

## II. INSTRUMENTATION AND EXPERIMENT DESCRIPTION

IWRAP, initially described in [7], is a dual-frequency conically scanning Doppler radar developed by the Microwave Remote Sensing Laboratory (MIRSL) at UMass that is routinely installed on a NOAA WP-3D research aircraft. IWRAP is primarily designed to study the signature of the ocean surface under wind forcing. The two radars (one C-band and one Ku-band) each nominally scan at multiple incidence angles, usually between 20° and 50°. Each radar is capable of implementing up to four simultaneous beams; however, two simultaneous beams per radar is the normal mode of operation. Both V and H polarizations are available on transmit and receive and are selected based upon mission requirements. For the Winter 2015 experiment, the C-band antenna spinning system was disabled. Its polarization switch was configured to measure VV, HH, VH, and HV polarizations by toggling rapidly between pairs of co-polarization and cross-polarization. The Ku-band

radar collected copolarized NRCS (VV/HH) while conically scanning and was available for most of the flights.

The C-band antenna used for this experiment is a prototype for the scatterometer on the next-generation MetOp-SG satellites [8]. The antenna is a dual-polarized slotted waveguide fan-beam antenna, with an elevation main lobe beamwidth of approximately  $40^\circ$  centered at boresight [9]. It was designed and manufactured by RUAG Space Sweden to have a cross-polarization isolation of better than 40 dB across the main lobe. The elevation gain pattern is sloped such that the gain at the farthest incidence angle is approximately 5 dB higher than at the nearest incidence angle. The equivalent azimuthal beam width across the main lobe is approximately  $5^\circ$  at both polarizations. The IWRAP C-band center frequency was tuned to transmit at the antenna-nominal operating frequency of 5.3 GHz.

Due to time constraints before the Winter 2015 experiment, the antenna was mounted in the aircraft nadir direction,<sup>1</sup> with the side of the antenna with the higher gain on the right side of the aircraft. Since the antenna was not scanned in azimuth, the WP-3D aircraft performed  $360^\circ$  orbits toward the left (i.e., a negative roll angle) in order to obtain NRCS measurements at incidence angles from  $20^\circ$  to  $60^\circ$ . Locations of consistent ocean-surface winds were chosen for the orbit positions. At absolute roll angles of less than  $50^\circ$ , two  $360^\circ$  orbits were performed back to back in what will be referred to hereafter as an orbit or circle “set”; at absolute roll angles of  $50^\circ$  and  $60^\circ$ , three orbits were performed in a set. In total, over 130 orbits were performed at roll angles ranging from  $-25^\circ$  to  $-60^\circ$ .

At a typical radar altitude of 7000 ft over the incidence angle range observed, the location of the measurement ranges from approximately 0.75 to 6 km from aircraft nadir. However, the radius of the circle traced by the aircraft changed depending on roll angle. Thus, a sample taken from an incidence angle of, for example,  $40^\circ$  covers a different area on the ocean surface depending on if the roll angle is  $-30^\circ$  (larger area) or  $-50^\circ$  (smaller area). The approximate diameter of the circles, which depended on flight-level winds and roll angle, ranged from 1.5 to 8 km. The footprint of IWRAP on the ocean surface was therefore between 2.25 and 14 km. The orbits at roll angles of  $-60^\circ$  took 30 to 50 s to complete, whereas the orbits at  $-25^\circ$  roll angle took 100 to 180 s. Fig. 1 shows the flight track of one particular orbit set from 2015 January 20.

Surface wind speed was measured by global positioning system (GPS) dropwindsondes,<sup>2</sup> moored buoys, the Stepped Frequency Microwave Radiometer (SFMR), and IWRAP itself. The orbits were performed near a buoy whenever possible. When this was not possible (e.g., the flights into higher wind areas while following a storm), GPS dropsondes were deployed and SFMR sampled the ocean surface brightness temperatures  $T_b$ . The winds at flight level caused the aircraft to drift from its original position during the orbit; therefore, after exiting the

<sup>1</sup>In actuality, the antenna was mounted with a  $-2^\circ$  pitch with respect to the aircraft. During level flight, the aircraft typically pitches up  $1.5^\circ$  to  $2.5^\circ$  to maintain altitude. This pitch difference was accounted for in the incidence angle calculation.

<sup>2</sup>In this paper, dropwindsondes are also referred to as dropsondes.

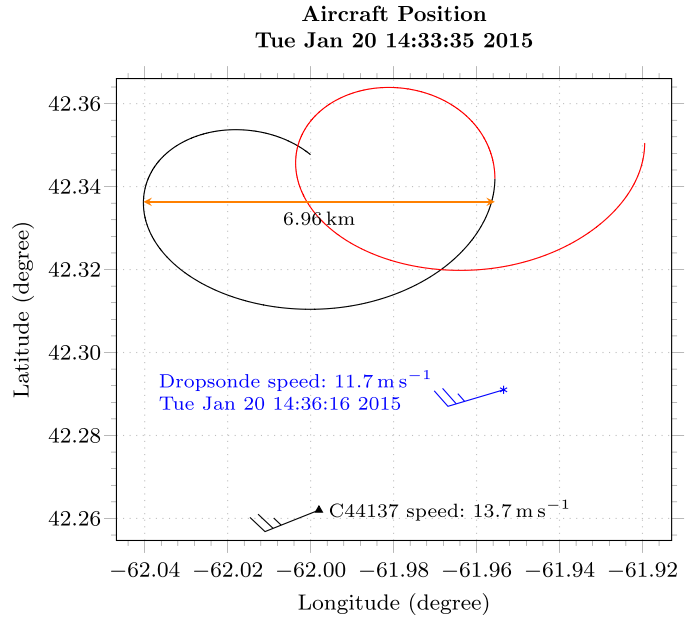


Fig. 1. Sample orbit set at  $-30^\circ$  roll from January 20, 2015. The triangle marks the buoy (C44137) location and the asterisk marks the GPS dropsonde splash location. The buoy speed is interpolated in time; therefore, the time associated with the buoy measurement is the same as the start time of the circular orbit. The GPS dropsonde was launched immediately before rolling into the first circle; therefore, its splash time was a few minutes later. The flight track is shown as a continuous solid line. The first complete circle of the set (left) is colored black, whereas the second circle (right) is colored red. The distance shown is the distance on the ocean surface from the minimum longitude of the first orbit to the maximum longitude of the second orbit.

roll, a return track was chosen such that the SFMR would sample the ocean covered during the maneuver. More information about the ground-truth sources is presented in Section III-D. Ultimately, wind speed retrievals from IWRAP C-band VV-polarized NRCS are found to be the most reliable source and are used for developing C-band VH and HH geophysical model functions in Section IV.

### III. DATA PROCESSING METHODOLOGY

During the Winter 2015 experiment, the IWRAP radars sampled the ocean surface with a sequence of 126 pulses in each of two polarization configurations (e.g., VV polarization for one sequence, VH polarization for the next, and so on). Typically, the C-band radar was configured for VV/VH mode during one orbit set and HH/HV mode during the next set at the same nominal roll angle. Raw in-phase and quadrature (I and Q) channel samples were collected and recorded. In postprocessing, these data were subject to pulse compression; Doppler spectrum moments were then accumulated over each 126-pulse block using pulse-pair methods [10]. The resulting profiles of backscatter and Doppler velocity are available at a rate of approximately 60 Hz per polarization. These profiles were then merged with navigation parameters (pitch, roll, drift, etc., available at a 50-Hz rate).

Once merged, the data are sorted by incidence angle into  $1^\circ$  bins and Earth-relative azimuth angle into  $5.625^\circ$  bins. The incidence angle is derived from navigation parameters and antenna azimuth information using methods described in [11].

### A. NRCS Calculation

The NRCS is estimated from the return echo using a pulse-limited illuminated surface area given an estimate of the absolute transceiver gain function provided by an internal calibration loop and the gain patterns provided by RUAG. Although 126 points are averaged to obtain an NRCS estimate, the number of independent samples is approximately 7 to 8. The integrated azimuthal beamwidths at each polarization and each antenna elevation angle between  $-15^\circ$  and  $15^\circ$  were derived by integrating over the  $-20$  dB points in the azimuth radiation patterns. These beamwidths were then used to compute the area illuminated by the antenna at all polarization combinations.

After averaging the NRCS azimuthally to obtain the mean NRCS, a small modulation was observed in comparison with the CMOD5.h GMF [12] as a function of antenna elevation angle. This is most likely a result of how the antenna was mounted (the mounting structure) or an effect of the radome and fairing structure. Using the procedure described in Appendix A, a correction was derived from mean NRCS data and the CMOD5.h GMF that was then applied to the gain pattern at each polarization.

### B. Calibration

While significant effort was made to perform an end-to-end system calibration on the ground prior to and after the Winter 2015 experiment, a residual NRCS offset (bias) was observed between the VV-polarized data and the existing C-band GMFs derived from ASCAT NRCS for winds where good agreement is expected ( $\leq 14$   $\text{ms}^{-1}$ ). In order to remove this offset, the following calibration procedure was performed to align the data to an existing GMF in the mean over a range of incidence angles and wind speeds. Since the goal of this paper is to analyze the behavior of NRCS at nonnadir incidence angles, all data used here are from orbits with an absolute roll angle of greater than  $15^\circ$ , which will minimize any contamination from the nadir surface echo.

First, Global Data Assimilation System (GDAS) model data [13] were interpolated in time and space (latitude and longitude) to the starting time and position of each set of circles. The collocated GDAS winds provide a surface reference from which the NRCS using the calibration GMF, CMOD5.h [12], is generated.

Since CMOD5.h was designed to operate between  $16^\circ$  and  $66^\circ$ , an incidence angle in this range ( $50^\circ$ ) was chosen for calibration. A least-squares fit was performed to the data (in linear space) from each circle to the following form:

$$\sigma^0 = A_0(1 + a_1 \cos \chi + b_1 \sin \chi + a_2 \cos 2\chi + b_2 \sin 2\chi) \quad (1)$$

where  $\sigma^0$  is the NRCS and  $A_0$ ,  $a_n$ ,  $b_n$ , and  $\chi$  are parameters that are allowed to vary as necessary. The peak of the fit is taken as the upwind direction. If the GDAS direction disagrees with the data by more than  $\pm 90^\circ$ , which occurred in less than 11% of the data, upwind is shifted by  $180^\circ$ .

The data arrays from each circle are then rotated such that the estimated upwind lies at  $0^\circ$ . A fit is then performed to the data

from each circle to the more traditional NRCS formulation, i.e.,

$$\sigma^0 = A_0(1 + a_1 \cos \chi + a_2 \cos 2\chi) \quad (2)$$

where  $\chi$  is now the wind-relative azimuth. The difference between each NRCS fit in azimuth and the GMF are then calculated. The median of all such differences in the calibration data set is the calibration offset—approximately 1.1 dB with a standard deviation of 0.2—and is applied to all data at all polarizations. This part of the procedure assumes that the differences between polarizations have been completely accounted for during ground calibration. In the IWRAP system, the only differences between VV and HH polarizations are the small insertion loss differences of the waveguide adapters, semirigid cables to the polarization switch, and the switch itself. The differences in the former two components at each polarization are small (on the order of tenths of a decibel), and the insertion loss of the polarization switch was measured and included in the NRCS calculations.

### C. Polarization Mixing Correction

When rotating the aircraft away from level pitch and roll, the instantaneous Earth incidence and azimuth angles can be determined from pitch and roll measurements of the WP-3D aircraft. If the electric field radiating from the antenna is not exactly perpendicular or parallel to the plane of the ocean, some mixing between V and H polarizations can occur. Since the antenna was mounted  $90^\circ$  to the right of the nose of the aircraft, the rotation angle of the electric field  $\gamma$  is simply the negation of the aircraft pitch angle (see (B17) in Appendix B).

The measured cross-polarized NRCS  $\sigma_{\text{VH}}^0$  is contaminated by copolarized NRCS due to the nonideal aircraft attitude. However, with good estimates of  $\sigma_{\text{VV}}^0$  and  $\sigma_{\text{HH}}^0$  this contamination can be removed. The amount of contamination can be expressed (in linear units) by

$$\sigma_{\text{VH}}^{\prime 0} = \sigma_{\text{VH}}^0 + (\sigma_{\text{VV}}^0 + \sigma_{\text{HH}}^0) \sin^2 \gamma \cos^2 \gamma \quad (3)$$

where the prime symbol indicates the measured quantity. This result is more fully explained in Appendix B.

To correct  $\sigma_{\text{VH}}^{\prime 0}$  for polarization mixing, the second copolarization term of (3) may be subtracted. Since both VV and HH NRCSs were not available at the same  $\gamma$  angles as were the VH NRCS during this experiment, we use modeled VV NRCS from CMOD5.h and apply the polarization ratio model from [2] to obtain modeled HH NRCS. This correction is then calculated at the VH  $\gamma$  angles and applied to VH NRCS for all profiles measured. For most of the cross-polarized NRCS (95%), the correction is less than 3.5% of the measured NRCS, i.e.,  $0.965 \sigma_{\text{VH}}^{\prime 0} < \sigma_{\text{VH}}^0 \leq \sigma_{\text{VH}}^{\prime 0}$ . The maximum value of the correction for this 95% of the data is  $6.3 \times 10^{-4}$ . A similar correction is performed for copolarized NRCS.

Since the pitch of the antenna is the most significant influence of  $\gamma$ , its uncertainty affects the observed NRCS. It is assumed that the largest error in pitch comes from the mounting angle of the antenna relative to the measured aircraft pitch; this is at most  $1^\circ$ . While this would affect all measurements, the VH NRCS is most affected at the lowest incidence angles (where the ratio

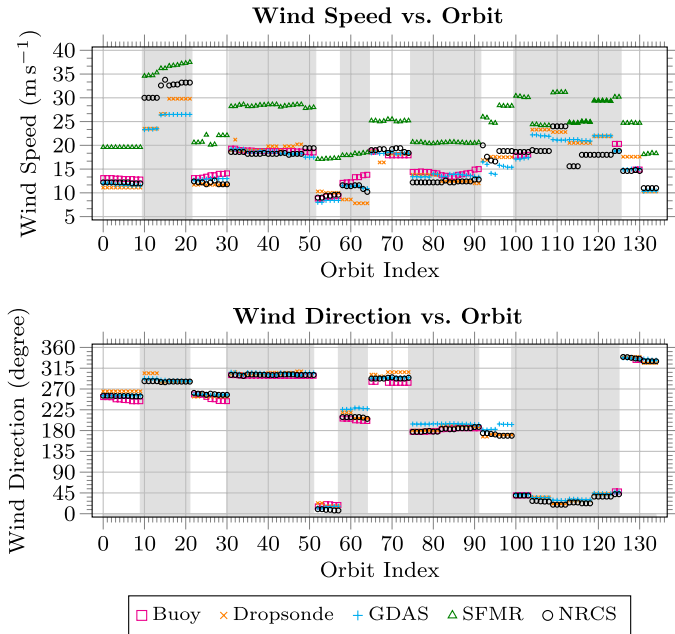


Fig. 2. Ground-truth comparisons for VV orbits. Flights are separated by gray and white backgrounds. The top panel is the wind speed from collocated ground-truth sources as a function of orbit number for the entire Winter 2015 experiment. The bottom panel is the wind direction for the same orbits. SFMR retrievals are biased high for the entire experiment. A filled SFMR symbol indicates a rain rate retrieval of at least  $2 \text{ mm h}^{-1}$ . It was confirmed visually that these orbits were in precipitation. Wind direction estimates from all sources generally agree.

$\sigma_{VV}^0/\sigma_{VH}^0$  is the largest). At these incidence angles, the undesired copolarized contribution would be at most 14 dB below the cross-polarized level. This amount of error would introduce an approximate 0.15-dB error in the mean measured VH NRCS and would vary slightly over azimuth. The amount of variation of CMOD5.h in azimuth is approximately 3 dB at  $15 \text{ ms}^{-1}$  and  $20^\circ$  incidence—the approximate maximum of the normalized second harmonic of VV-polarized NRCS. This would create a false azimuthal variation of approximately 0.3-dB peak to peak, which is negligible compared with the amount of variability in the observed NRCS attributed to fading alone.

#### D. Ground-Truth Selection and Collocation

During the Winter 2015 experiment, a variety of ocean-surface vector wind “truth” sources were available (see Fig. 2). Four different moored buoys (C44024, C44137, C44139, and C44141) were near the operational area of most flights. These report 10-min-averaged wind vectors measured at a height of 5 m (except for C44024, which is at 4 m) every hour. The wind speeds provided are simple scalar averages, and the wind direction is derived via the arctangent of the  $u$  and  $v$  component averages. The time provided with the buoy data is actually the time that the wave-parameter averaging begins, which is 35 min before meteorological parameter averaging begins. Therefore, the time used for interpolation is 35 min later than the time provided with the buoy data.

C44137, C44139, and C44141 have two anemometers: one propeller/wind vane type (the “primary” sensor) and one ultrasonic type (the “secondary” sensor). The former is accurate to

$\pm 0.3 \text{ ms}^{-1}$  (up to  $30 \text{ ms}^{-1}$ ) in wind speed and  $3^\circ$  in direction; the latter is accurate to  $\pm 3\%$  of the wind speed reading and  $\pm 2^\circ$  in direction. Following [14], data were eliminated whenever the two sensors disagreed by more than  $2.5 \text{ ms}^{-1}$  or at least  $30^\circ$ . The amount of data eliminated from these buoys for all of January and February was less than 0.2%. For most of these data, the difference in wind speeds between the two sensors was less than  $\pm 1 \text{ ms}^{-1}$ , and the difference in wind directions was between  $-15^\circ$  and  $0^\circ$ . In general, the secondary anemometer measured slightly higher wind speeds and directions that were more clockwise than the primary (i.e., the distributions for the differences “primary–secondary” are skewed negative). The direction difference could be explained by a misalignment or miscalibration to true North of either of the two sensors. The wind speed and direction from the primary propeller-based sensor was chosen to represent buoy winds in this analysis after being filtered using the additional data from the secondary sensor.

For each orbit of the WP-3D aircraft, the closest buoy in distance (within 50 km) was selected. It is worth noting that flights around a buoy were performed when relatively uniform wind conditions were expected near the buoy. When two valid measurement reports existed within  $\pm 1 \text{ h}$  of the orbit, the wind vector components were interpolated in time to the start time of the orbit. When only one valid measurement existed, which occurred for ten orbits, that wind vector was used as is. Finally, all collocated buoy winds were converted to 10-m equivalent neutral winds ( $U_{10N}$ ) according to Liu *et al.* [15].

A total of 50 GPS dropwindsondes were deployed from the WP-3D during the experiment. The closest dropsonde in time to the beginning of each orbit set was chosen for collocation as long as it did not exceed the time threshold (30 min) and distance threshold (30 km). According to an error analysis by Hock and Franklin [16], the winds derived from dropsondes are expected to have an accuracy level of  $0.5$  to  $2 \text{ ms}^{-1}$ . To reduce the influence of wind gusts, the surface wind vector at 10 m ( $U_{10}$ ) from each dropsonde was obtained by using an altitude-weighted average of the lowest 150 m of measurements available between 10 and 350 m to simulate continuous samples, referred to as WL150. The fall rate is a function of atmospheric pressure; therefore, it took the dropsondes between 11.5 and 19 s to fall through the 150-m layer. To convert WL150 to  $U_{10}$ , the empirically derived conversion equation from Uhlhorn *et al.* [17] is used

$$U_{10, \text{dropsonde}} = 0.85 \text{ WL150} + 0.89. \quad (4)$$

For each dropsonde, the  $u$  and  $v$  components were individually converted to 10-m winds using (4). The results were converted to a  $U_{10N}$  vector using the lowest dropsonde-measured relative humidity, ambient atmospheric pressure, and ambient temperature, and sea-surface temperature (SST) from the same database used for the reprocessed SFMR retrievals. As in hurricanes, these results are still not an ideal representation of the sustained wind vector. This scaled layer average is intended to convert an inherently smoothed Lagrangian wind measurement to a Eulerian equivalent near the surface [18]. This does not necessarily result in a larger spatial scale represented by the measurement, but it does simulate a fixed anemometer at the surface.

The SFMR was available for all flights. Since the design frequency of the RUAG/ESA antenna was so close to the second-to-lowest SFMR frequency (5.31 GHz), SFMR data on this channel were corrupted during every flight. To obtain wind speeds from SFMR,  $T_b$  from only the highest four frequencies are used to retrieve the final wind speed and rain rate. Quality-controlled aircraft data (e.g., radar altitude and ambient temperature) and modeled ocean SSTs and salinities are used for SFMR reprocessing, in order to utilize the most recent retrieval algorithms and to avoid errors due to mismatched real-time data from the aircraft. As an example of the latter problem, a few seconds lag in real-time data on the aircraft to the SFMR processor (which is typical) can result in some measured  $T_b$  at a roll angle larger than desired. Errors in the SFMR retrievals due to SST and salinity are minimized by using models (NOAA/NCDC AVHRR Daily-OI-V2 and HYCOM GLBa0.08, respectively) for the time and location nearest to each point in the flight. The recently revised excess emissivity and rain algorithms from [19] were used to perform the retrievals.

Although SFMR measurements were available during the circle patterns, the retrieval algorithm is only reliable near nadir incidence. To collocate SFMR with NRCS measurements, all  $T_b$  and auxiliary parameters within 25 km and 60 min of each orbit set were collected. The wind speed and rain rate were retrieved from the mean of these  $T_b$  and aircraft parameters and were used as the SFMR measurements for the orbit set. Compared with the other ground-truth sources, SFMR wind speeds were biased high for every flight. While the exact cause is uncertain, the SFMR concept is most robust at winds greater than  $15 \text{ ms}^{-1}$  where there is a closer correlation between fractional foam coverage and local wind speed on the sea surface. Because of this uncertainty, no correction was attempted for the SFMR retrievals at this time. Due to the clear bias and that SFMR retrievals do not provide any information about ocean surface wind direction, the SFMR data are omitted from the remaining analysis.

Buoy and dropsonde measurements were available for many of the patterns, but they were not always at the exact location being sampled by IWRAP (due to aircraft drift during the orbit or sensor motion, for example). The outputs of both the buoy and dropsonde sensors are ultimately the mean of a few point measurements in time and space. Numerical models, such as GDAS, are generally coarse estimates of the mean winds and do not perform that well at higher wind speeds. However, since there are VV-polarized NRCS samples near each orbit, wind vector retrievals from VV C-band NRCS orbits can also be used as a ground-truth source. The distinct advantage of this method is that collocated VV NRCS measurements were taken on the same spatiotemporal scale as the other polarization configurations (i.e., they best represent VH and HH measurements). In the following results, these retrievals are used to group NRCS by wind speed, but first, some justification is provided.

### E. Ground-Truth Validation

Mean NRCS from the CMOD5.h GMF was generated for wind speeds from 0.2 to  $50 \text{ ms}^{-1}$  in  $0.2\text{-ms}^{-1}$  steps and

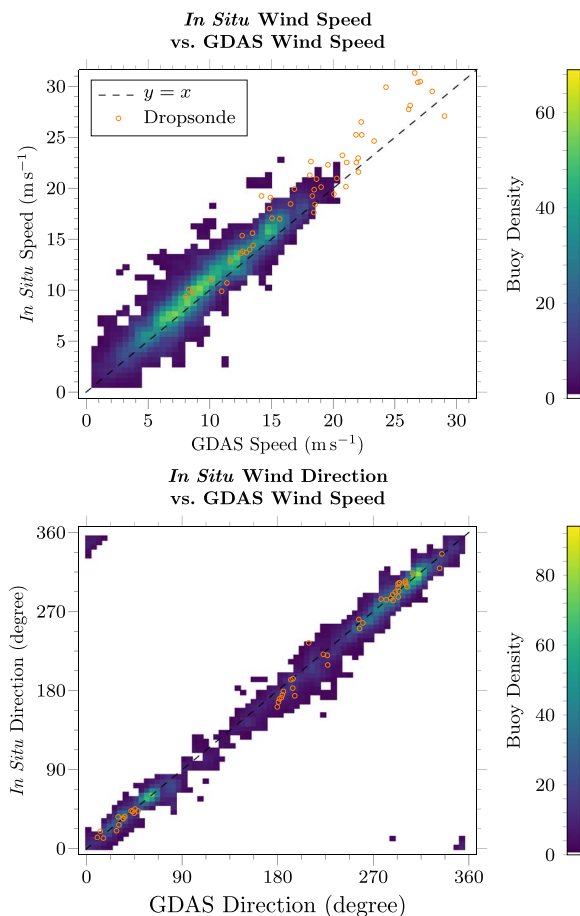


Fig. 3. *In situ* equivalent neutral wind speed as a function of GDAS wind speed (top panel) and wind direction (bottom panel). Buoys are represented by the 2-D histogram contour, and dropsondes are represented by empty blue circles. For each measurement by an *in situ* sensor, the GDAS wind speed was interpolated to the time and location of the sensor. Buoy data are all available measurements from all buoys near WP-3D flights in January and February 2015. On average, the buoy winds are biased slightly high compared with GDAS. All dropsonde data are from the Winter 2015 experiment and exhibit a slight high bias.

incidence angles from  $26^\circ$  to  $66^\circ$  in  $1^\circ$  steps. To collocate a wind vector with a circle pattern, all VV-polarized NRCS from within  $\pm 20$  km from the orbit start position and  $\pm 45$  min of the orbit were averaged together within each incidence angle and wind-relative azimuth bin. The resulting data are azimuthal scans for each incidence angle bin that contains an NRCS measurement. The wind speed for the orbit was retrieved by minimizing the differences from estimates of the mean NRCS ( $A_0$ ) at all incidence angles with the GMF. The wind speed with the smallest total difference (in linear units) is considered the wind speed of the orbit. Each VV orbit has a wind direction associated with it that is estimated from the NRCS, as described in Section III-B. The retrieved wind direction is the mean direction from all NRCS direction estimates in the box. Here, these retrievals will be compared with other collocated ocean surface wind vector estimates.

All buoy measurements taken during January and February 2015 from the buoys listed in Section III-D were collocated with GDAS winds interpolated to the time and location of the buoy. The buoy winds were filtered and converted to  $U_{10N}$  as in Section III-D and plotted as a 2-D histogram in Fig. 3.



The same procedure (except for filtering) was done for GPS dropsondes dropped by the WP-3D during the Winter 2015 experiment. These points are plotted as empty circles in Fig. 3. Overall, the two *in situ* measurements show good agreement with GDAS in both wind speed and direction. The dropsondes sampled higher wind speeds than the buoys did; approximately 40% of dropsondes sampled at least  $20 \text{ ms}^{-1}$ , whereas almost no buoys sampled winds this high. The larger apparent scatter at higher winds is consistent with other analyses involving a much larger number of dropsondes [17], [19].

The residual of each *in situ* measurement with GDAS (i.e.,  $U_{10N, \text{GDAS}} - U_{10N, \text{in situ}}$ ) were binned into  $0.5\text{-ms}^{-1}$  wind speeds and  $2.5^\circ$  wind directions and plotted as histograms in Fig. 4. The buoy residual distributions are shown as solid black bars, whereas the dropsonde residual distributions are shown as hatched bars. These plots show more clearly that, on average, both buoy and dropsonde wind speeds are biased slightly high with respect to GDAS. The wind directions both agree relatively well with GDAS.

The VV NRCS retrievals collocated with each circle were then compared to buoys, dropsondes, and GDAS wind speeds collocated at each circle. As described earlier, these winds are retrieved from an average of the NRCS from nearby individual circles in time and space. Since the NRCS was calibrated using GDAS winds, the retrievals should agree—at least at low wind speeds—relatively well with GDAS. Based on observations of Fig. 4, the retrieved wind speeds should be lower than both buoy and dropsonde wind speeds in the mean.

Fig. 5 shows the averaged VV retrievals that were collocated with an orbit as a function of buoy, GPS dropsonde, and GDAS wind speeds collocated with the same orbit. The  $y = x$  line is shown as a dashed line. There are a few areas on Fig. 5 that seem to have a constant VV-retrieval response to changes in *in situ* measurements, i.e., the GDAS, dropsonde, or buoy wind speed changes, whereas the retrieved wind speed does not change significantly. This appears most obviously at VV-retrieved wind speeds of approximately  $12$  and  $18 \text{ ms}^{-1}$ . Often, this indicates a spatial or time variation captured by the ground-truth samples that is not representative of the ocean-surface wind vector. However, that does not seem to be the case here as there is no dependence of VV-retrieved wind speed residual on time or distance of ground truth from the aircraft. This effect is attributed to uncertainty in the measurements—which includes the wind sampling precision, collocation errors, spatiotemporal representation errors, and, specifically in the case of dropsondes, conversion to surface winds.

As an example of the variation of surface wind speeds with time, Fig. 6 shows surface wind speed estimates from VV retrievals and all ground-truth sources for the flight on February 1, 2015. All trends are generally the same for the entire two-hour flight time shown, although an outlier does stand out: The dropsonde near 1450Z is almost  $2 \text{ ms}^{-1}$  lower than the next nearest collocated dropsonde. All other measurements are approximately within the  $18\text{--}20 \text{ ms}^{-1}$  range.

Since GDAS winds, dropsondes, and buoys were collocated with each orbit at VV polarization, a triple collocation analysis [20] was used to assess which data set matched best with the VV retrievals. Since there were only 17 orbits with all

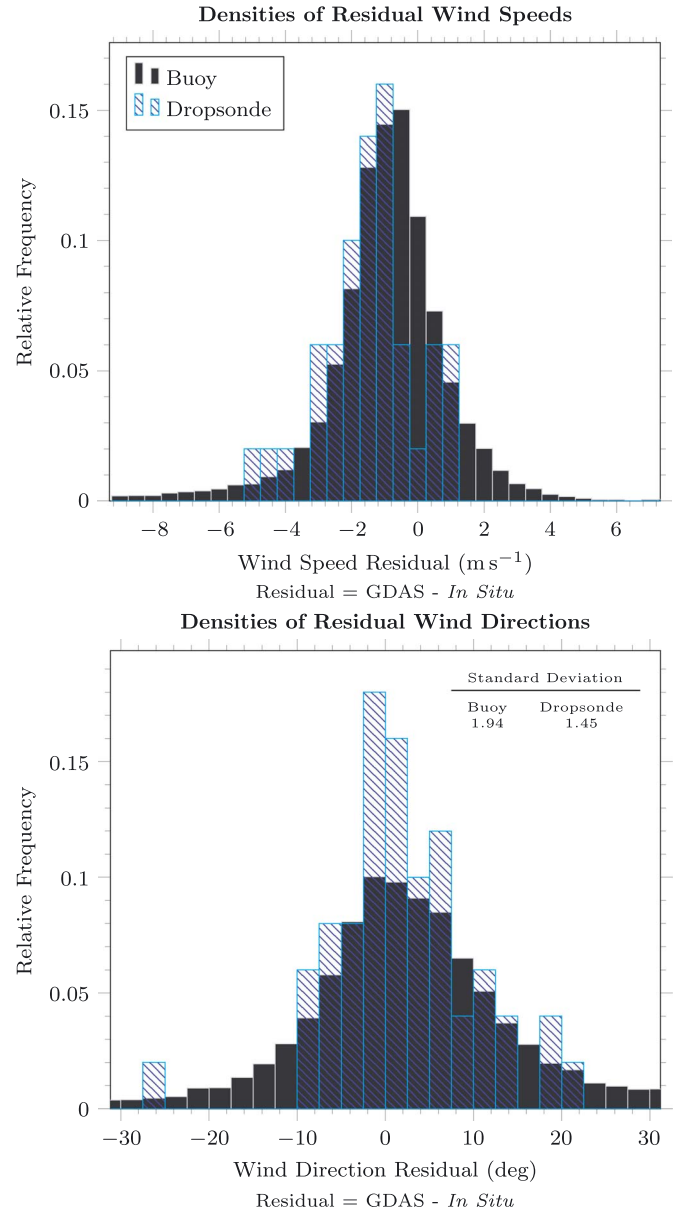


Fig. 4. Histogram of residuals of GDAS wind speed less *in situ* wind speed (top panel) and GDAS wind direction less *in situ* wind direction (bottom panel). Buoys are represented by solid black bars, and dropsondes are represented by shaded blue bars. For each measurement by an *in situ* sensor, the GDAS wind speed was interpolated to the time and location of the sensor. *In situ* data that were at least  $25 \text{ ms}^{-1}$  were eliminated to avoid contaminating the density plots with high winds in which GDAS is not expected to perform well. The upper panel suggests that buoy wind speeds are biased slightly high and dropsonde wind speeds agree well with GDAS. The wind speed and direction errors appear to be similar for both buoys and dropsondes.

ground-truth sources, reliable intercalibration of each source is not possible; however, general comparisons can still be made. The GDAS model is valid over large scales (hundreds of km and a few hours); therefore, it does not resolve smaller scale features. However, due to the consistent wind fields chosen for this experiment, these features are not expected to have a significant impact. Here, it is estimated that buoys, dropsondes, and the scatterometer all resolve the surface wind vector on a similar spatial and temporal scale. Each wind vector was broken into orthogonal components and compared with two

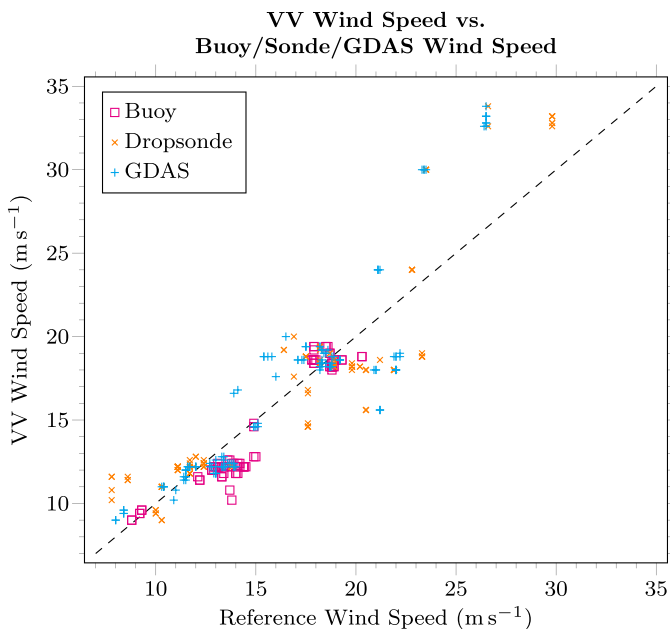


Fig. 5. VV-polarization NRCS wind speed retrievals as a function of buoy, GPS dropsonde, and GDAS wind speeds. Buoys are shown as empty circles, dropsondes are shown as  $\times$  symbols, and GDAS winds are shown as  $+$  symbols. The  $y = x$  line is shown as a dashed line.

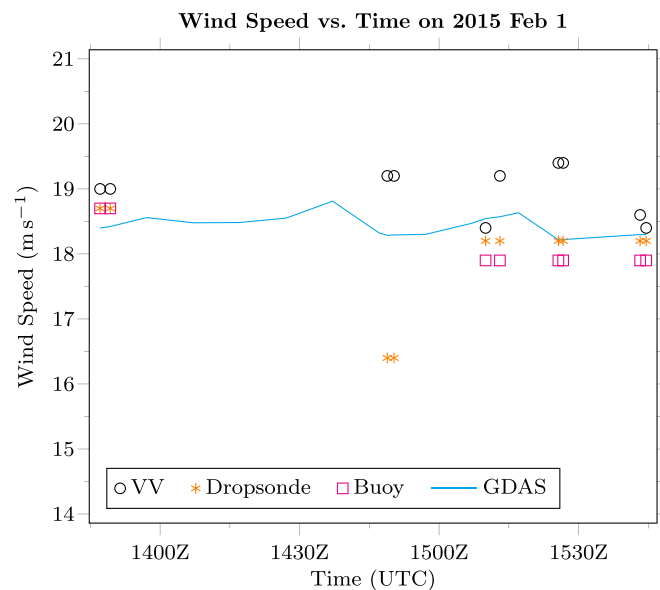


Fig. 6. Wind speed time series from the flight on February 1, 2015 for the ground-truth sources used in the Winter 2015 experiment. Empty circles show VV retrievals, asterisks show GPS dropsonde surface wind estimates, and empty squares show time-interpolated buoy measurements. The solid line is GDAS interpolated in space and time to the location of the aircraft. The general trends for all wind speed sources are consistent over the measurement time.

other sources, one of which was always GDAS since it likely has the largest spatiotemporal scale. The error standard deviations were computed as in [20] to obtain an estimate of the random measurement error with respect to the scales resolved by GDAS.

Since there were not many collocations, the representation error variance ( $r^2$  in [20] and [21]) was not estimated or used here. As a result, the error standard deviations are on the scale

TABLE I  
ERROR STANDARD DEVIATIONS DERIVED FROM A TRIPLE COLLOCATION ANALYSIS OF BUOYS, DROPSONDES, AND GDAS-MODELED POINTS FROM THE WINTER 2015 EXPERIMENT. THESE ARE PRESENTED ON THE COMMON SCALE OF THE BUOY, DROPSONDE, AND SCATTEROMETER FROM THE PERSPECTIVE OF THE GDAS SCALE

Reference System	Buoy ( $\text{m s}^{-1}$ )		VV ( $\text{m s}^{-1}$ )		Sonde ( $\text{m s}^{-1}$ )	
	u	v	u	v	u	v
Buoy	2.099	2.812	1.951	2.506		
Dropsonde			0.953	2.377	1.430	2.853

of the buoys, dropsondes, and scatterometer. The VV retrievals appeared to compare better with dropsondes than with buoys for the triple collocation data set, but this does not include any winds above  $20 \text{ m s}^{-1}$ . This suggests that the VV retrievals best represent dropsondes on the scales of GDAS, although with a total wind-speed error standard deviation on the order of  $2.5 \text{ m s}^{-1}$ . Table I shows the error standard deviations calculated from this triple collocation data set with different “reference systems” (i.e., the system which would be the calibration reference for the other two).

## IV. RESULTS AND ANALYSIS

### A. GMF Development

The CMOD5.n model function [22] was developed as the latest adjustment in a long history of C-band VV-polarization model functions in the CMOD family [23]. The most recent revision, CMOD5.n was developed to remove an observed  $0.5\text{-ms}^{-1}$  underestimation of wind speed retrievals from the ERS scatterometer. CMOD5 is claimed to increase the maximum wind speed capability of the GMF to  $35 \text{ m s}^{-1}$  [24]. However, Vogelzang *et al.* [20] report a 1%–2% underestimation of wind speeds retrieved from ASCAT at all wind speeds, compared with buoys. Soisuvarn *et al.* [12] also report a low bias in ASCAT retrievals for wind speeds above  $10 \text{ m s}^{-1}$  when compared with winds retrieved from QuikSCAT. They developed a model function based on a hybrid of CMOD5.n and the saturation wind speed of the IWRAP GMF [1] to take advantage of the remaining sensitivity observed in the ASCAT NRCS measurements. They did not alter the performance of the GMF below  $10 \text{ m s}^{-1}$  or the directional retrieval accuracy, only the mean NRCS at higher wind speeds. CMOD5.h was implemented as a lookup table and not as a continuous function; therefore, a parametrization for a cross-polarization GMF based on CMOD5.h is not possible. However, CMOD5.n is a parameterized function of incidence angle, azimuth, and wind speed; therefore, its formulation was chosen as the basis for the cross-polarization GMF developed here.

CMOD5.n uses a slightly different model for NRCS than described by (2) with respect to the wind-relative azimuth  $\chi$

$$\sigma^0(\chi) = \left( \sum_{i=0}^2 B_{iz} \cos(i\chi) \right)^{1.6}. \quad (5)$$

The subscript  $Z$  indicates the coefficient is from the “ $z$ -space” formulation, which is simply a transformation of variable in which  $z = (\sigma^0)^{1/1.6}$ , as opposed to the traditional NRCS space.

TABLE II  
COEFFICIENTS FOR THE CROSS-POLARIZATION (VH) GMF

Parameter	Value	Parameter	Value
$c_1$	-1.7669	$c_{15}$	$1.2475 \cdot 10^{-3}$
$c_2$	-0.4568	$c_{16}$	0.7825
$c_3$	-0.0232	$c_{17}$	-0.0268
$c_4$	-0.1313	$c_{18}$	28.4490
$c_5$	0.0000	$c_{19}$	2.0813
$c_6$	$4.0000 \cdot 10^{-3}$	$c_{20}$	3.0000
$c_7$	0.0796	$c_{21}$	5.9726
$c_8$	0.0236	$c_{22}$	-2.3302
$c_9$	7.0859	$c_{23}$	1.8631
$c_{10}$	3.0792	$c_{24}$	5.4622
$c_{11}$	-2.2077	$c_{25}$	4.8271
$c_{12}$	1.2820	$c_{26}$	1.5940
$c_{13}$	0.0153	$c_{27}$	3.4385
$c_{14}$	0.0486	$c_{28}$	2.2216

TABLE III  
COEFFICIENTS FOR THE HH-POLARIZATION GMF

Parameter	Value	Parameter	Value
$c_1$	-0.9615	$c_{15}$	$3.6878 \cdot 10^{-3}$
$c_2$	-1.0636	$c_{16}$	0.4181
$c_3$	0.2886	$c_{17}$	$7.0071 \cdot 10^{-3}$
$c_4$	-0.1115	$c_{18}$	30.3620
$c_5$	0.0000	$c_{19}$	2.0813
$c_6$	$4.0000 \cdot 10^{-3}$	$c_{20}$	3.0000
$c_7$	0.1086	$c_{21}$	11.8860
$c_8$	$9.8148 \cdot 10^{-4}$	$c_{22}$	0.1404
$c_9$	7.0216	$c_{23}$	2.5895
$c_{10}$	3.5257	$c_{24}$	3.0010
$c_{11}$	-1.6794	$c_{25}$	-1.1215
$c_{12}$	-9.6963	$c_{26}$	0.6898
$c_{13}$	-9.9208	$c_{27}$	2.5220
$c_{14}$	0.1423	$c_{28}$	-0.3425

After a third-order Taylor expansion, and ignoring harmonics greater than the second

$$\sigma^0(\chi) \approx B_{0z}^{1.6} (1 + 1.6 H(\chi) + 0.48 H^2(\chi)) \quad (6)$$

where  $H(\chi) = b_{1z} \cos(\chi) + b_{2z} \cos(2\chi)$  [25]. For each polarization, a function in the form of (6) was fit to the NRCS observations while retaining the CMOD5.n parameterization. The Levenberg–Marquardt technique was used to perform a least-squares fit to the binned NRCS observation cube (incidence angle, upwind-relative azimuth, and wind speed) described in Section III. The parameters were initialized with the CMOD5.n coefficients [22], and all were allowed to vary as needed to reduce the  $\chi^2$  error, except those chosen *a priori* ( $c_5$  and  $c_6$ ) and those tuned by eye to match the observed behavior in light winds ( $c_{19}$  and  $c_{20}$ ). These parameters do not have much of an effect on the resulting GMF.  $c_5$  was only included in CMOD5 to allow for future tuning and was set to 0. The lowest winds observed in this experiment were  $8 \text{ ms}^{-1}$ ; therefore, the behavior in light winds is undefined regardless of  $c_{19}$  and  $c_{20}$ . Table II lists the coefficients for the VH GMF. A similar procedure for HH polarization was followed, and the coefficients for the HH GMF are listed in Table III.

### B. Behavior of NRCS With Wind-Relative Azimuth

Fig. 7 shows the cross-polarized (VH) NRCS as a function of wind-relative azimuth for all wind speeds observed at  $50^\circ$

incidence. The empty circles are the averaged values for the particular wind speed, wind-relative azimuth, and incidence angle bins. An error bar indicates one standard deviation of the NRCS data within the bin. The solid line on top of the data is the derived GMF at the center wind speed of each bin. The dash-dotted line is CMOD5.h at the center wind speed of each bin, with the scale indicated on the right side of the plot. Each panel shows a  $2\text{-ms}^{-1}$  wind speed range between 8 and  $34 \text{ ms}^{-1}$ .

The data shown in Fig. 7 indicate dependence of the cross-polarized NRCS on wind-relative azimuth. Similar to the copolarized NRCS, the amplitude of the modulation decreases as wind speed increases, with the directional signature becoming very small above  $20 \text{ ms}^{-1}$ . Compared with the azimuthal response of CMOD5.h (which is the same as CMOD5.n), there is less of directional dependence at all wind speeds observed. In the  $14\text{-ms}^{-1}$  bin, there appears to be some higher harmonics present in the azimuthal signature, but this is likely due to geophysical noise. In this particular wind speed bin, the VH NRCS (at this incidence angle) were sampled from two consecutive orbits, with both exhibiting similar azimuthal variation.

While these observations of wind direction dependence may appear to be at odds with some recent cross-polarization observations [2], [3], [5], [26], others suggest that slight azimuthal dependence exists [4], [27]–[30]. Based on observations at other frequency bands (e.g., L-band [31] and Ku-band [32]), it has been expected that C-band measurements would be similarly affected by wind-direction-relative azimuth angle.

The azimuthal modulation presented here is from  $50^\circ$ , which, if it exists, has been shown to have a higher amplitude than that from lower incidence angles. When comparing the results of [5] with similar data from  $35^\circ$  at 18 and  $20 \text{ ms}^{-1}$  (not shown), we note an approximate 2-dB variation of mean NRCS over azimuth. Since this is on the same order as the standard deviations at each azimuth angle of the median VH data presented in [5]; the two data sets may be consistent within the margins of error.

The theoretical model of Fois *et al.* [6] provides for some amplitude modulation in VH NRCS due to scattering from a rough ocean surface. The predicted modulation is stronger at higher wind speeds than the Winter 2015 data show, but it is approximately on the same order of magnitude. The only example that can be compared is at a wind speed of  $25 \text{ ms}^{-1}$ , where “the peak-to-peak scattering modulation of VH polarization is about  $\dots 2 \text{ dB}$  at  $37.5^\circ$ .” While the Winter 2015 data have a smaller modulation at this wind speed and incidence angle (not shown; approximately 1 dB), the maximum peak-to-peak difference observed is approximately 3 dB (between 8 and  $15 \text{ ms}^{-1}$ ). The differences with the model of [6] are well within the margins of error of the IWRAP measurements.

It is impractical to show all incidence angle and wind speed bins such as those in Fig. 7; therefore, the data and GMFs will be broken down into the harmonics of (2):  $A_0$ ,  $a_1$ , and  $a_2$ . The effects of wind speed on each harmonic will be examined further in the following.

### C. Incidence Angle Behavior

Fig. 8 shows the incidence angle dependence between  $20^\circ$  and  $60^\circ$  of the mean NRCS ( $A_0$  term) for all polarizations



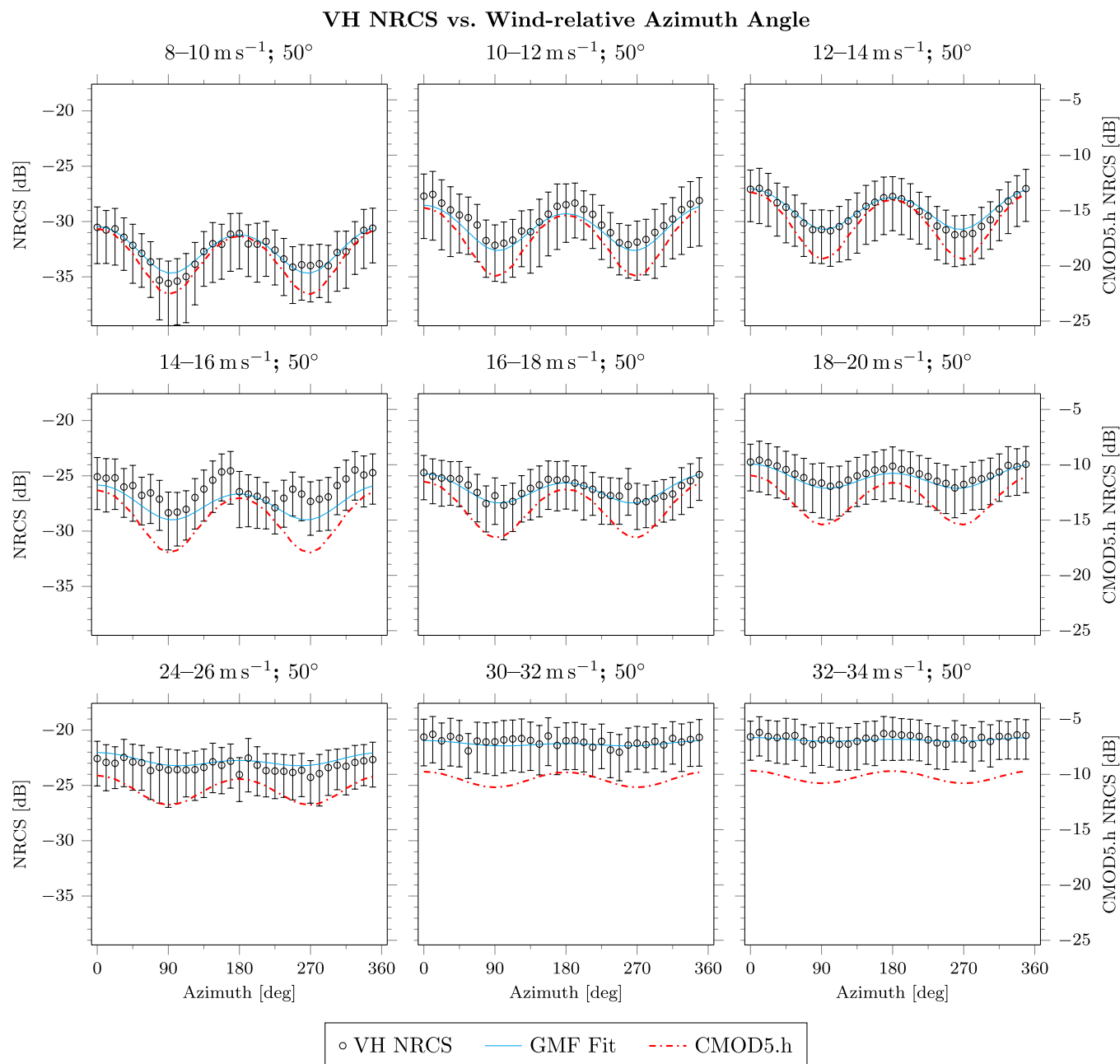


Fig. 7. Cross-polarized (VH) NRCS as a function of wind-relative azimuth at an incidence angle of 50°. Empty circles are the mean NRCS, whereas error bars show one standard deviation of the data within the azimuth, wind speed, and incidence angle bin. The new VH GMF is shown as a solid line, and the CMOD5.h GMF (which is a VV-polarization GMF) is shown as a dash-dotted line.

and wind speeds observed during the Winter 2015 experiment. Missing points at higher incidence angles are a result of a lack of orbits performed at absolute roll angles greater than 40° in those wind conditions. The mean  $A_0$  within each incidence angle and wind speed bin is shown as the symbol indicated in the legend, and error bars are shown for each bin with multiple orbits contributing to it. An error bar for a given point is one standard deviation of  $A_0$  estimates derived from each orbit at that particular incidence angle and wind speed bin. The solid lines show CMOD5.h and the dash-dotted lines show the ECMWF-based model from [5] for the center wind speeds of each panel. This latter model, henceforth referred to as Z-2014-E, was developed using RADARSAT-2 images of hurricanes from

20° to 50° incidence and ECMWF-modeled winds as ground truth.

The VV-polarized data follow the trend of CMOD5.h in all wind speed bins. This is expected since retrievals from VV  $A_0$  are used to determine wind speed. The HH-polarized  $A_0$  behaves as expected, generally matching VV  $A_0$  at lower incidence angles. Above 30° to 40° incidence, the HH  $A_0$  deviates from the VV trend, with less power being scattered back toward the radar for the same wind speed. The two cross-polarized data sets lie almost on top of each other, suggesting that there is no difference between VH and HV NRCS at the wind speeds observed. Where they do differ (e.g., at wind speeds below 16 ms<sup>-1</sup>), it is possible they are observing spatial surface wind

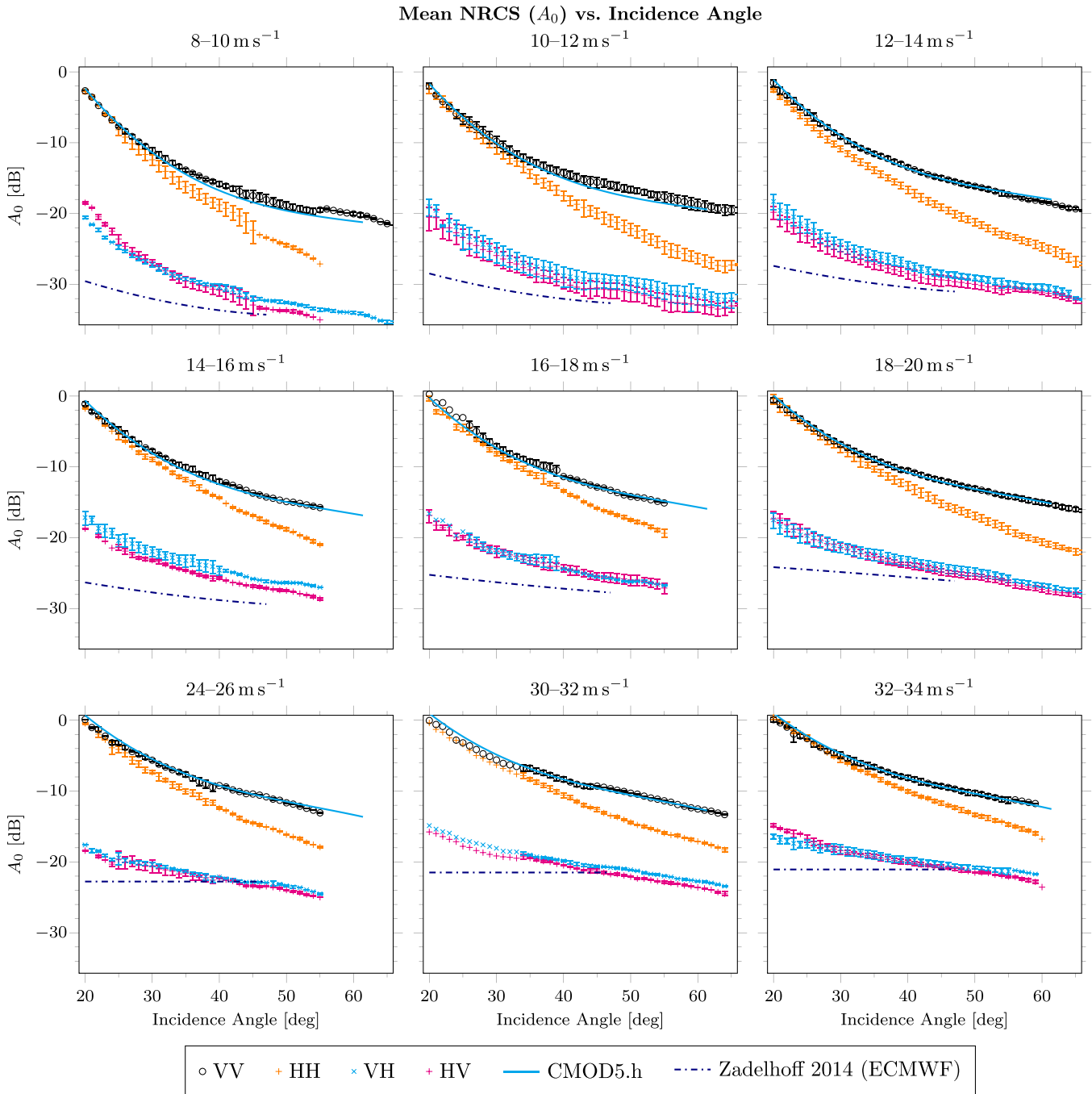


Fig. 8. Mean NRCS ( $A_0$ ) as a function of incidence angle for all wind speeds observed during the Winter 2015 experiment. Incidence angles range from  $20^\circ$  to  $60^\circ$ . The solid lines show CMOD5.h, and the dash-dotted lines show the ECMWF-based model from [5] from  $20^\circ$  to  $50^\circ$  for the center wind speeds of each panel. Panels without data from all polarization combinations are not shown.

variation. The VH and HV samples were taken at different times and locations due to the sampling method required by IWRAP. In particular, at the shallower roll angles, which took up to 10 min to complete one orbit set, the two polarizations could be observing a different ocean state. Therefore, only the VH-polarized NRCS is analyzed in the remainder of this paper.

The Z-2014-E model predicts a small incidence angle dependence of cross-polarized  $A_0$  up to  $20 \text{ ms}^{-1}$ , beyond which they did not have enough data to draw a conclusion. The observations presented here indicate greater dependence on incidence

angle than predicted by this model. There is smaller dependence of NRCS on incidence angle at the higher wind speeds, but it is still measurable. The slopes of the  $A_0$  measurements are steeper at lower wind speeds, which matches the behavior of Z-2014-E. Differences between Z-2014-E and the observed VH NRCS may be a result of the limited number of samples in [5]. The data presented in Fig. 8 suggest that the incidence-angle-dependent physical processes were not completely captured by the RADARSAT-2 images. It is unclear why the vertical offset between the data and models are present.

### Mean VV and VH NRCS ( $A_0$ ) vs. Wind Speed

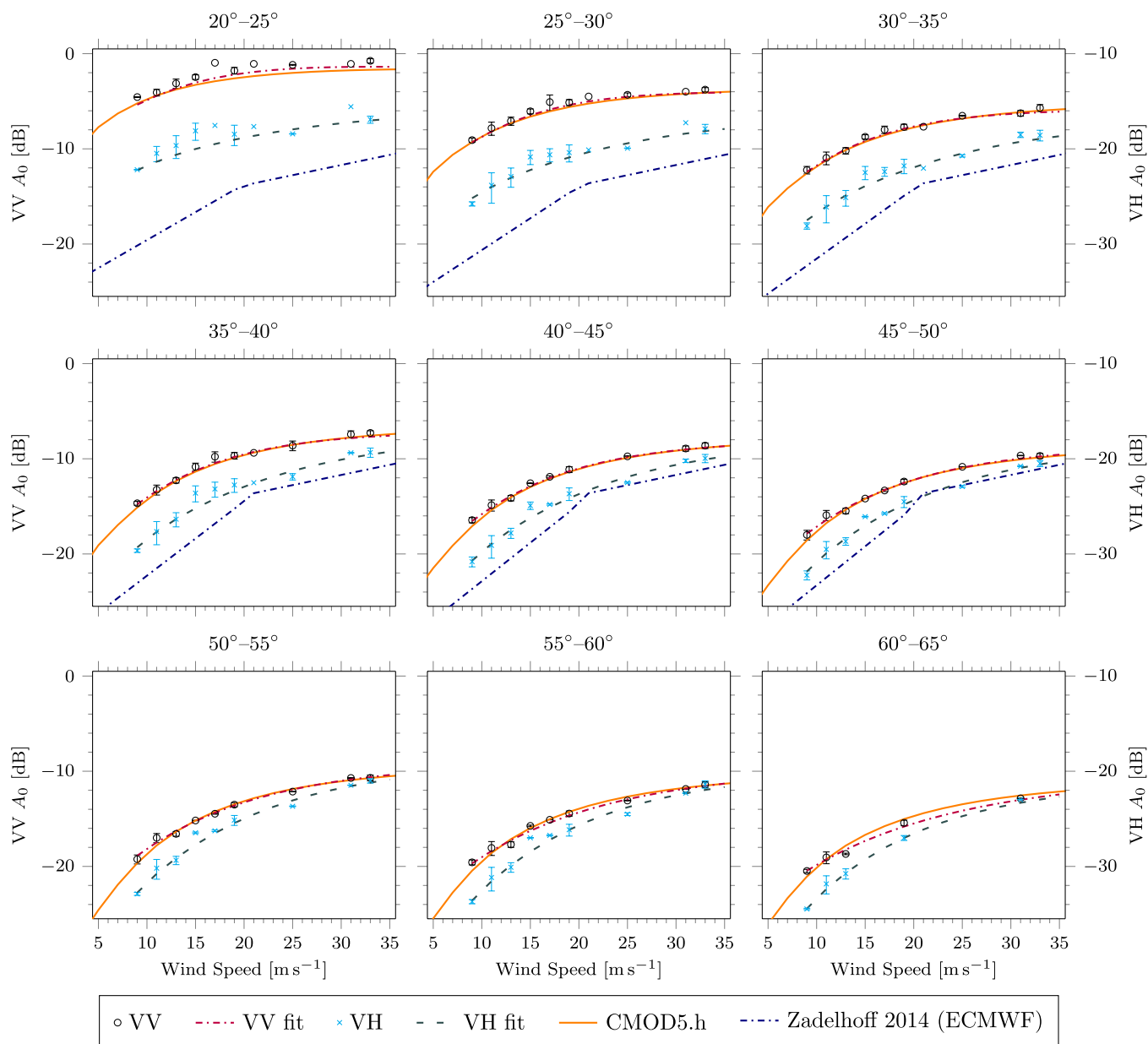


Fig. 9.  $A_0$  as a function of wind speed. The data from an average of five incidence angles is shown for VV and VH polarizations as filled circles and X symbols, respectively. CMOD5.h for the center incidence angle is shown as a solid line. The model from [5] at the center incidence angle of each panel is shown as a dashed line at all incidence angles. Models derived from the data for VV and VH are shown as dash-dotted and long-dashed lines, respectively. An error bar for a given point is one standard deviation of  $A_0$  estimates derived from all orbits at the particular incidence angle bins and wind speed bin.

#### D. Wind Speed Behavior on GMF Harmonics

It is often informative to break the components of the observed NRCS into the harmonics described by (2). Since CMOD5.n, and thus, this paper, uses a slightly different model for NRCS than (2), a method of transformation needs to be developed. Reducing the terms of (6) to single harmonics, Stoffelen and Anderson [25] obtain an NRCS equation with five harmonics

$$\sigma^0(\chi) \approx A_0 \left( 1 + \sum_{i=1}^4 a_i \cos(i\chi) \right). \quad (7)$$

The highest four harmonics are defined as

$$a_1 = 1.6b_{1z} + 0.48b_{1z}b_{2z} \quad (8)$$

$$a_2 = 1.6b_{2z} + 0.24b_{1z}^2 \quad (9)$$

$$a_3 = 0.48b_{1z}b_{2z} \quad (10)$$

$$a_4 = 0.24b_{2z}^2. \quad (11)$$

The values  $a_3$  and  $a_4$  are small; therefore, they are neglected in the following discussion. For the purposes of comparing the new cross-polarization GMF with the properties of the traditional formulation (e.g.,  $a_1$  is the normalized upwind/downwind difference), the transformation described in (7) to (9) is used here.

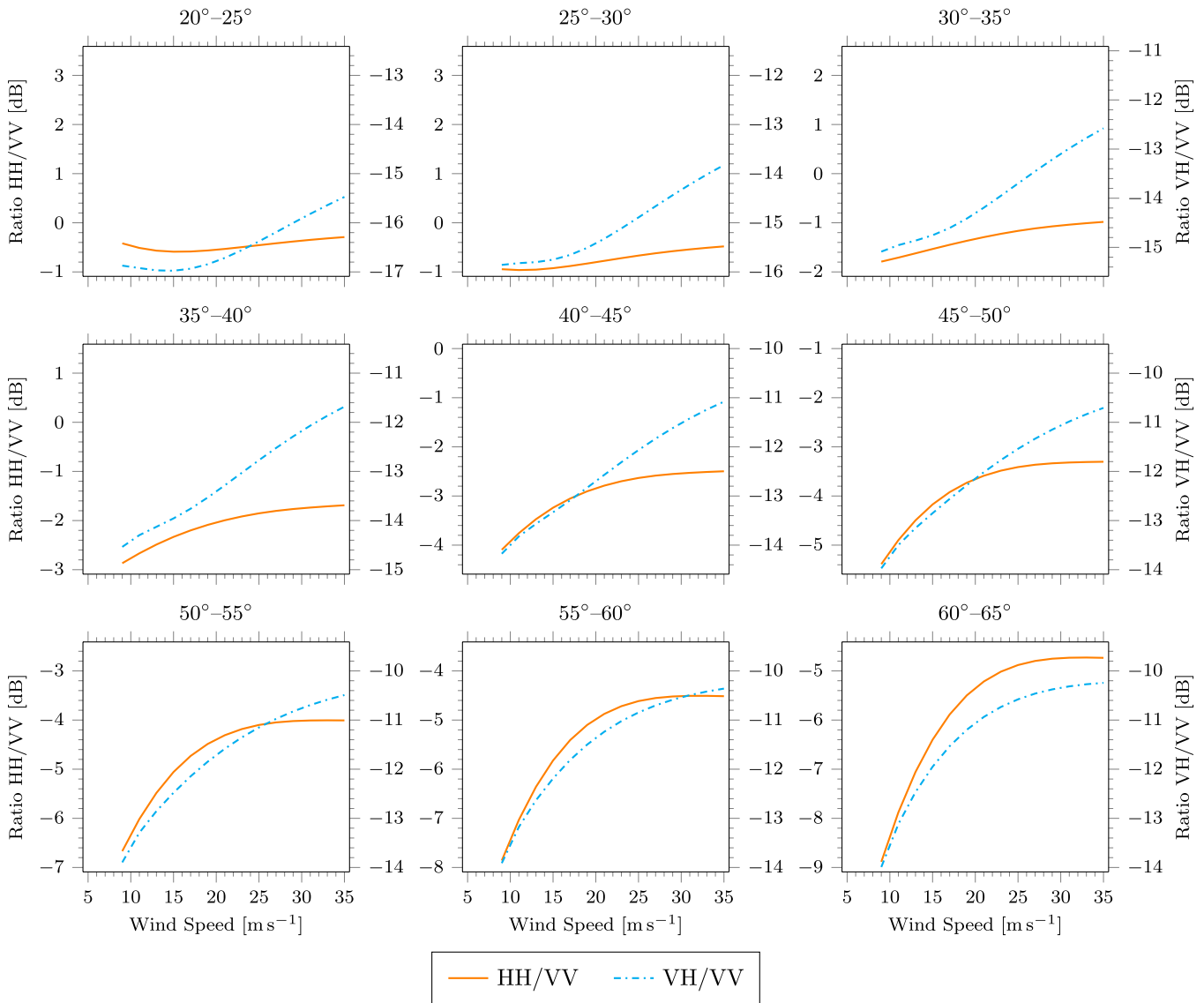
Mean NRCS ( $A_0$ ) Ratio vs. Wind Speed

Fig. 10. Polarization ratios (in decibels) of mean NRCS ( $A_0$ ) as a function of wind speed. The ratios between the models derived from the Winter 2015 data are shown as solid (HH/VV) and dash-dotted (VH/VV) lines from the center of the incidence angle bin indicated. The co-polarization ratio axis is on the left of each panel and the cross-polarization ratio axis is on the right; both axes have the same range. The minimum value of each panel's vertical axes were chosen independently such that the entire range of polarization ratios would fit in the plot. As the ratio increases, the numerator approaches the denominator (VV). When the slope of the ratio is positive, which occurs for almost all wind speed ranges of both polarizations, the sensitivity of the polarization to wind is better than that at VV polarization. VH polarization has a better sensitivity to wind speed above  $20 \text{ ms}^{-1}$  than does VV.

Fig. 9 shows  $A_0$  as a function of wind speed over the range of incidence angles observed. In each panel, the data from an average of five incidence angles is shown for VV and VH polarizations. The  $A_0$  from CMOD5.h is shown as a solid line above  $25^\circ$  and as a dashed line below. The  $A_0$  from the VV and VH models are shown as dash-dotted and long-dashed lines, respectively; the VV model closely follows, and is sometimes obscured by, the CMOD5.h trend. An error bar for a given point is one standard deviation of the  $A_0$  estimates derived from all orbits at the particular incidence angle bin and wind speed bin. The VH  $A_0$  model is similar to that of VV, but at an amplitude of approximately 10–18 dB less depending upon the incidence angle (note the different scales for VV and VH  $A_0$ ). This can be more clearly observed in Fig. 10. At the lower incidence angles,

the cross-polarization ratio VH/VV is closer to  $-15 \text{ dB}$  across the wind speed range observed. The sensitivity of VH  $A_0$  to wind speed at all incidence angles is more than that of VV and is more apparent at lower wind speeds.

Polarization ratios for both co-polarization and cross-polarization GMFs are shown in Fig. 10. When the slope of the ratio HH/VV or VH/VV is positive, the sensitivity of the polarization in the numerator is better than VV polarization for the same wind speed range. Comparing the slopes of the two polarization ratios, it can be observed that VH-polarization has better sensitivity to wind speed than either VV or HH polarization above  $20 \text{ ms}^{-1}$ . Notably, the VH polarization ratio is increasing at all incidence angles shown up to the maximum observed wind speeds, whereas the HH ratio generally flattens



VV and VH  $a_1$  vs. Wind Speed

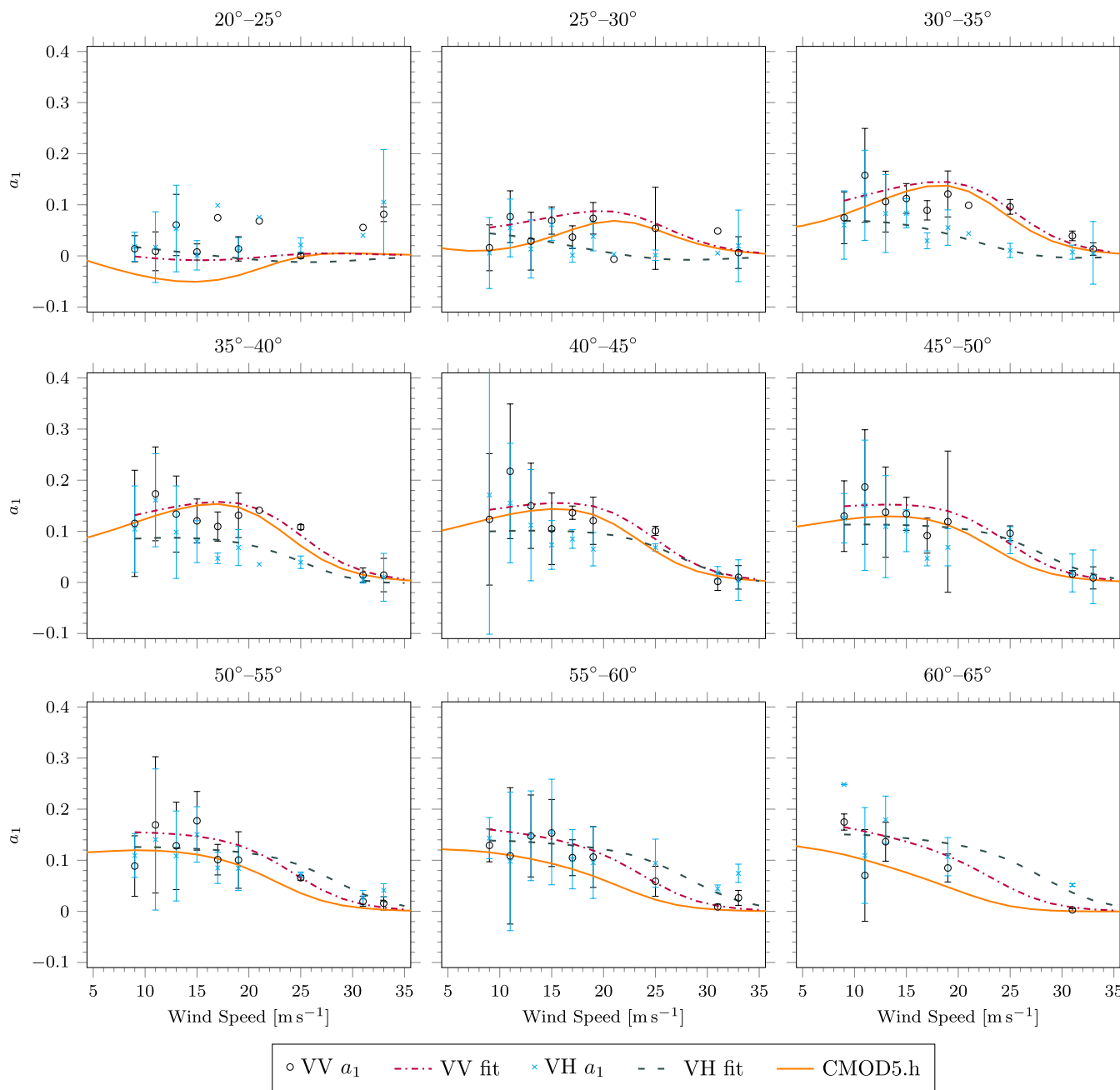


Fig. 11.  $a_1$  as a function of wind speed. The data from an average of five incidence angles is shown for VV and VH polarizations as filled circles and X symbols, respectively. CMOD5.h is shown as a solid line above 25° and a dashed line below. Models for VV and VH are shown as dash-dotted and long-dashed lines, respectively. An error bar for a given point is one standard deviation of  $a_1$  estimates derived from all orbits at the particular incidence angle bins and wind speed bin.

out above 25 ms<sup>-1</sup>. This suggests that the VH  $A_0$  is not yet saturating at these wind speeds. However, the increase in cross-polarization NRCS with wind speed compared with co-polarization is still modest at best.

Fig. 11 shows  $a_1$  as a function of wind speed over the range of incidence angles observed. In each panel, the data from an average of five incidence angles is shown for VV and VH polarizations. The  $a_1$  from CMOD5.h (which is the same as CMOD5.n) is shown as a solid line above 25° and as a dashed line below. The  $a_1$  from the VV and VH models are shown as dash-dotted and long-dashed lines, respectively; the VV model

closely follows the CMOD5.h trend. An error bar for a given point is one standard deviation of the  $a_1$  estimates derived from all orbits at the particular incidence angle bin and wind speed bin.

The  $a_1$  parameter in the traditional NRCS GMF formulation controls the upwind/downwind difference. At the lowest incidence angles, 20° to 25°, the  $a_1$  amplitude is relatively flat. CMOD5.h predicts that the downwind peak is higher than upwind below 25 ms<sup>-1</sup> (i.e.,  $a_1$  is negative), whereas the data indicate otherwise. Determination of the wind direction from NRCS first assumes that  $a_1$  is positive, but the result can be

VV and VH  $a_2$  vs. Wind Speed

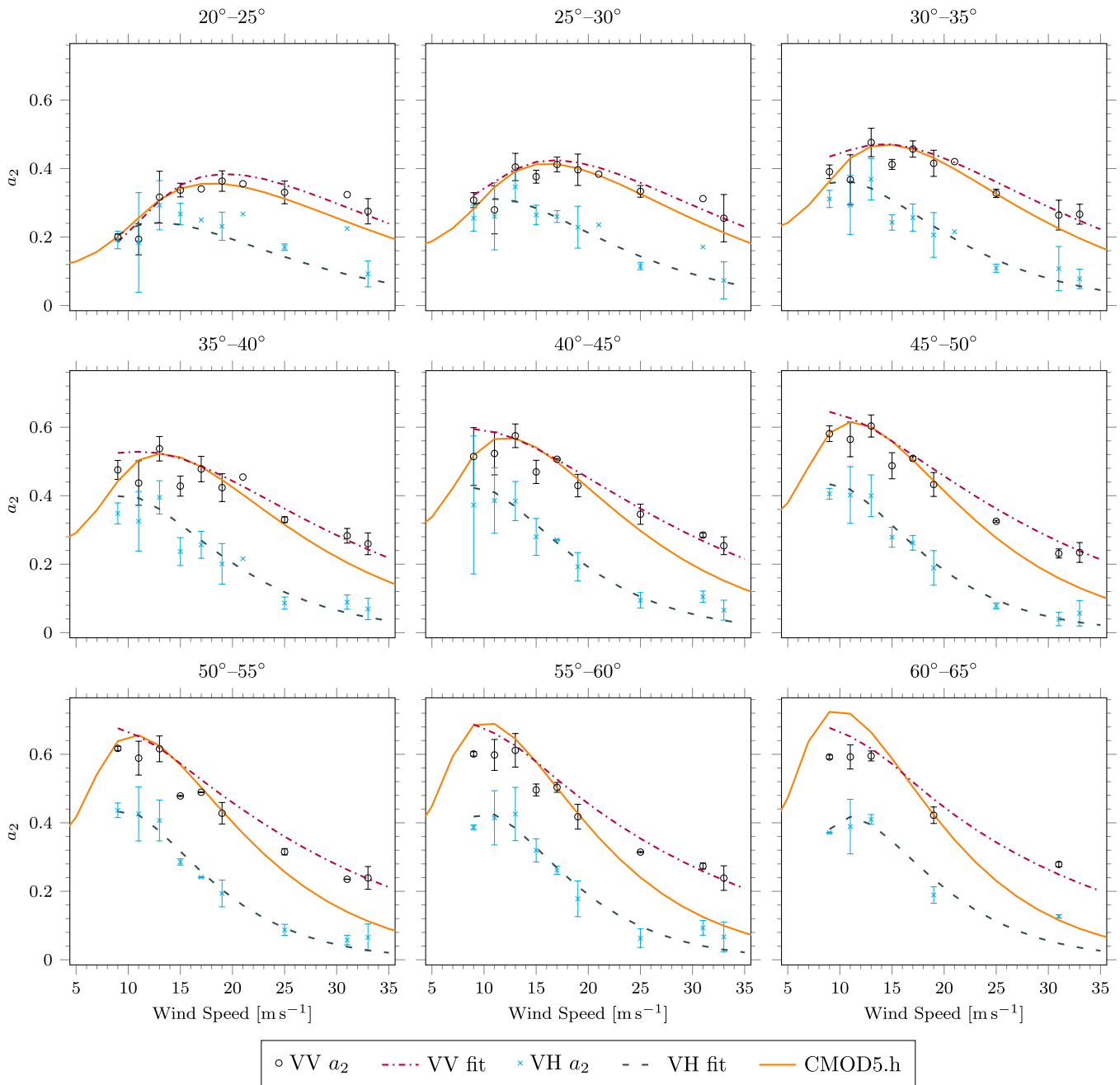


Fig. 12.  $a_2$  as a function of wind speed. The data from an average of five incidence angles are shown for VV and VH polarizations as filled circles and X symbols, respectively. CMOD5.h is shown as a solid line above 25° and as a dashed line below. Models for VV and VH are shown as dash-dotted and long-dashed lines, respectively. An error bar for a given point is one standard deviation of  $a_2$  estimates derived from all orbits at the particular incidence angle bins and wind speed bin.

corrected by 180° if GDAS winds indicate otherwise. Based on Fig. 11 and the comparison between *in situ* observations and the retrieval results in Fig. 2, this assumption appears to be valid. The data indicate that  $a_1$  for VV and VH are close in this incidence angle range, nearly flat, and likely at least 0. This means that the upwind and downwind NRCS peaks are approximately the same amplitude.

Between incidence angles of 35° to 50°, the difference between upwind and downwind NRCS peaks is the greatest. Up to 35° incidence, the cross-polarized  $a_1$  is almost insensitive

to wind speed, whereas the VV response is a stronger function of wind speed. Up to 45° incidence, the VH  $a_1$  has a smaller amplitude than VV. The general trend at both co-polarization and cross-polarization is that this parameter decreases as wind speed increases, reaching 0 by approximately 30  $\text{m s}^{-1}$ . At incidence angles above 45° to 50° the VH upwind/downwind difference appears to be greater than that of VV at wind speeds above 20  $\text{m s}^{-1}$ , but more observations are needed to confirm this.

Fig. 12 shows  $a_2$  as a function of wind speed over the range of incidence angles observed. The data are arranged in the same

way as for  $A_0$  and  $a_1$ . This parameter is closely related to the upwind/crosswind difference and is indicative of the flatness of the NRCS signature over azimuth. In all the panels, the VH response to wind speeds above  $15 \text{ ms}^{-1}$  has a similar shape as the fitted VV model. This suggests that the cross-polarization upwind/crosswind response is similar to that of co-polarization (VV), but with diminished amplitude. This feature manifests itself in Fig. 7 as a curve that is smaller peak to peak across all wind speeds than the copolarized equivalent.

Where it exists, the initial increase in  $a_2$  with wind speed is slightly different between the copolarized and cross-polarized measurements. The low incidence angle data (i.e., between  $20^\circ$  to  $35^\circ$ ) suggest that the peak upwind/crosswind difference occurs at a lower wind speed than VV polarization. At these angles, the VV  $a_2$  peaks at nearly the same wind speed as predicted by CMOD5.h. However, the VH  $a_2$  show a peak at a lower wind speed than at VV, at perhaps 5 to  $15 \text{ ms}^{-1}$  compared with 15 to  $20 \text{ ms}^{-1}$ . There is not enough low-wind data for the curve fit to appropriately model this feature at the higher incidence angles and lower wind speeds; therefore, it is not clear if this trend continues as the wind speed decreases. However, this suggests that cross-polarized NRCS may be as useful for retrieving wind direction below  $10 \text{ ms}^{-1}$  and below  $40^\circ$  incidence as copolarized NRCS when the scatterometer system is sensitive enough to measure the signal.

## V. SUMMARY

Data collected from a series of flight experiments performed with the IWRAP airborne scatterometer over the North Atlantic Ocean in January and February 2015 has been described. IWRAP was operated in such a way as to measure the cross-polarized NRCS of the ocean surface at C-band in winds between 8 and  $34 \text{ ms}^{-1}$ . This was made possible by using a new antenna that has a high cross-polarization isolation, developed for ESA by RUAG Space Sweden and loaned to NOAA for this experiment. Surface wind speeds were obtained from moored buoys, GPS dropwindsondes, the GDAS model, and the SFMR. Ultimately these sources were used to validate retrievals from the copolarized (VV) NRCS, which was then used as the ground truth for analyzing the cross-polarized NRCS. The C-band antenna was mounted pointing toward nadir; therefore, many  $360^\circ$  orbits at fixed roll angles were performed to obtain NRCS measurements at incidence angles from  $20^\circ$  to  $60^\circ$  at all polarizations.

A cross-polarization GMF was developed using the CMOD5.h GMF as a basis. The cross-polarized NRCS shows measurable incidence angle dependence at wind speeds less than  $22 \text{ ms}^{-1}$ . There appears to be no difference between the VH and HV NRCS at the wind speeds and incidence angles sampled. The mean cross-polarization NRCS ratio VH/VV varies with incidence angle and wind speed, approaching  $-18 \text{ dB}$  at the smallest angles and  $-10 \text{ dB}$  at the largest angles. While there were limited samples at wind speeds near hurricane force, the data suggest that the sensitivity of the mean cross-polarized NRCS to wind speed is better than the copolarized  $A_0$  at the higher wind speeds. The cross-polarization NRCS ratio changes by approximately 1.5 to 4 dB over the wind speed range observed, depending on incidence angle. This indicates

some gain in ocean-surface wind speed sensitivity compared with VV polarization. The incidence angle range with the most opportunity for an improvement over co-polarization measurements seems to be between  $30$  and  $55$ . In this range, the VH  $A_0$  has a better sensitivity to changes in wind speed than VV at all wind speeds observed, and the VH signal does not show evidence of saturation.

The cross-polarized NRCS has weaker sensitivity to wind direction than copolarized NRCS, but it is still measurable. This azimuthal sensitivity does not appear to be an artifact of the copolarized contribution to the cross-polarized NRCS. The data indicate that the upwind NRCS peak in azimuth (at both co- and cross-polarization) is at least as large as the downwind peak, even at incidence angles as low as  $20^\circ$ . The upwind/crosswind difference, or flatness of the NRCS curve in azimuth, is similar at both co-polarization and cross-polarization. However, this difference is smaller for VH polarization than at VV polarization at almost all wind speeds measured during this experiment; the wind speed sensitivity is much stronger than the wind direction sensitivity. At winds below  $10 \text{ ms}^{-1}$  and incidence angles below  $40^\circ$ , the cross-polarized NRCS has a peak-to-peak amplitude that is nearly the same as VV NRCS. Although there are not many samples in this regime, the trend suggests that there are some situations at low winds in which the VH NRCS may have a larger upwind/crosswind difference than VV.

The data presented here indicate a few advantages of cross-polarization over co-polarization for ocean vector wind scatterometry. Assuming the combined transmitter power and receiver sensitivity of the scatterometer is good enough to sample the cross-polarized NRCS, the VH  $A_0$  has greater sensitivity to wind speed change than VV  $A_0$ . Although this is true for HH  $A_0$  as well, VH  $A_0$  appears to also be more sensitive to wind speed than HH. Particularly at incidence angles below  $55^\circ$ , the VH mean NRCS shows greater sensitivity to wind speed than HH. The VH NRCS is less sensitive to wind direction and is almost insensitive above  $24$  to  $26 \text{ ms}^{-1}$ . VH NRCS samples collocated with VV (as is planned for MetOp-SG) may reduce the uncertainty of ocean vector wind retrievals above  $24 \text{ ms}^{-1}$  to  $26 \text{ ms}^{-1}$  due to this insensitivity to direction and relatively greater sensitivity to wind speed. In order to verify this, more NRCS measurements at a variety of wind speeds above  $30 \text{ ms}^{-1}$  (e.g., in hurricanes) and upwind-relative azimuth angles are needed.

## APPENDIX A

### METHODOLOGY FOR ANTENNA PATTERN CORRECTION

During data processing, a small modulation in NRCS was observed with respect to the CMOD5.h GMF as a function of elevation angle. To correct for this effect, which was likely due to the antenna surroundings, orbits at roll angles from  $-25^\circ$  to  $-55^\circ$  for wind speeds less than or equal to  $14 \text{ ms}^{-1}$  were identified using the GDAS wind speeds collocated in the same manner, as described in Section III-B. At each aircraft-relative elevation angle at each of VV and HH polarizations, the mean NRCS was calculated from CMOD5.h and the GDAS wind speed. At HH polarization, the polarization ratio from [2] was applied to the CMOD5.h output since CMOD5.h is only

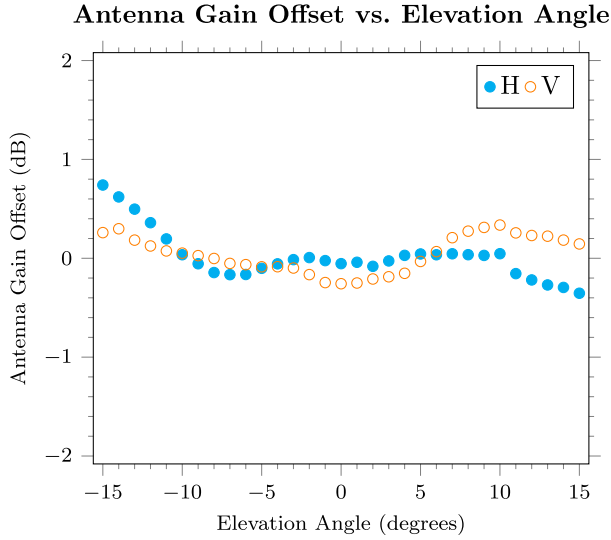


Fig. 13. Derived antenna gain offsets as a function of aircraft-relative elevation angle. Positive elevations are toward the right of the aircraft. Estimated H-polarization offsets are shown as filled circles, whereas empty circles show V-polarization offsets.

valid for VV polarization. The ratio between the GMF-modeled NRCS and the measured NRCS means at each elevation angle between  $-15^\circ$  and  $15^\circ$  off the antenna bore sight was calculated for each wind speed bin and nominal roll angle. Since the GDAS wind was scattered about the true surface wind, some small constant offsets were observed in these ratios between different wind speed bins. The ratios were normalized by the mean over each pattern to remove this effect. Finally, all these ratios were averaged within  $1^\circ$  (antenna-relative) elevation angle bins and were stored as the gain correction for the particular polarization. When calculating the NRCS, this correction was subtracted (in decibels) from the original gain pattern before applying it to the received power. As shown in Fig. 13, the applied offsets were less than  $\pm 1$  dB across the entire pattern for both V- and H-polarization antennas.

#### APPENDIX B POLARIZATION MIXING DERIVATION

Following Lee *et al.* [11], the aircraft-relative coordinate system is used with  $\hat{x}_a$  pointing over the right wing,  $\hat{y}_a$  toward the nose, and  $\hat{z}_a$  upward through the fuselage. For a conically scanning radar antenna, the unit vector in the propagation direction is

$$\hat{k} = \hat{x}_a \sin \theta_a \sin \phi_a + \hat{y}_a \sin \theta_a \cos \phi_a + \hat{z}_a \cos \theta_a \quad (\text{B12})$$

where  $\theta_a$  is the zenith angle measured from the positive  $z_a$ -axis and  $\phi_a$  is the azimuth angle measured clockwise from the  $y_a$ -axis (the aircraft heading). This is converted to a level track-relative coordinate system by successive rotations through the aircraft roll, pitch, and drift angles.

For the Winter 2015 flight experiments, the antenna was fixed with  $\phi_a$  at  $90^\circ$ . After rotation through a roll angle  $R$  and a pitch angle  $P$ ,  $\hat{k}$  becomes

$$\hat{k} = \hat{x}(\sin \theta_a \cos R + \cos \theta_a \sin R) + \hat{y} \sin \theta_a \sin P \sin R + \hat{z}(-\sin \theta_a \cos P \sin R + \cos \theta_a \cos P \cos R) \quad (\text{B13})$$

where the  $\hat{x}$ ,  $\hat{y}$ , and  $\hat{z}$  unit vectors now indicate a level Earth-relative coordinate system. The zenith angle of the radar beam on the sea surface is given by  $\cos \theta' = \hat{z} \cdot \hat{k}$ , or

$$\theta' = \cos^{-1}(-\sin \theta_a \cos P \sin R + \cos \theta_a \cos P \cos R) \quad (\text{B14})$$

which is the supplement of the incidence angle  $\theta$ .

The unit vector parallel to the  $H'$ -polarization in aircraft coordinates is the  $\hat{\phi}_a$  unit vector given by

$$\hat{\phi}_a = \hat{x}_a \cos \phi_a - \hat{y}_a \sin \phi_a = -\hat{y}_a \quad (\text{B15})$$

which when subjected to a roll angle  $R$  and a pitch angle  $P$  is expressed in level coordinates as

$$\hat{\phi} = -\hat{y} \sin \phi_a \cos P - \hat{z} \sin \phi_a \sin P. \quad (\text{B16})$$

The rotation angle of this vector out of the horizontal is given by

$$\begin{aligned} \tan \gamma &= \frac{\phi_z}{\sqrt{\phi_x^2 + \phi_y^2}} = \frac{-\sin \phi_a \sin P}{\sin \phi_a \cos P} \\ &= -\tan P. \end{aligned} \quad (\text{B17})$$

The received (complex) voltage at the antenna can be expressed by

$$\mathbf{V}_r = \mathbf{R} \mathbf{S} \mathbf{R} \quad (\text{B18})$$

where

$$\mathbf{R} = \begin{bmatrix} \cos \gamma & \sin \gamma \\ -\sin \gamma & \cos \gamma \end{bmatrix} \quad (\text{B19})$$

is the rotation matrix and

$$\mathbf{S} = \begin{bmatrix} S_{VV} & S_{VH} \\ S_{HV} & S_{HH} \end{bmatrix} \quad (\text{B20})$$

is the complex scattering matrix. For radar backscatter,  $S_{VH} = S_{HV}$  (i.e., scattering is reciprocal). Equation (B18) then becomes

$$\mathbf{V}_r = \begin{bmatrix} S_{VV} \cos \gamma + S_{VH} \sin \gamma & S_{VH} \cos \gamma + S_{HH} \sin \gamma \\ -S_{VV} \sin \gamma + S_{VH} \cos \gamma & -S_{VH} \sin \gamma + S_{HH} \cos \gamma \end{bmatrix} \mathbf{R}. \quad (\text{B21})$$

The power received by the radar at cross-polarization (VH) is the magnitude of the voltage squared

$$P_{r,VH} = V_{r,VH} V_{r,VH}^* \quad (\text{B22})$$

$$\begin{aligned} &= |S_{VH}|^2 + S_{VH} (S_{VV}^* + S_{HH}^*) \sin \gamma \cos \gamma \\ &\quad + S_{VH}^* (S_{VV} + S_{HH}) \sin \gamma \cos \gamma \\ &\quad + |S_{VV} + S_{HH}|^2 \sin^2 \gamma \cos^2 \gamma. \end{aligned} \quad (\text{B23})$$

Using the identity

$$S_1 S_2^* + S_1^* S_2 = 2 \operatorname{Re} \{ S_1 S_2^* \} = 2 \operatorname{Re} \{ S_1^* S_2 \} \quad (\text{B24})$$

it follows that:

$$\begin{aligned} P_{r,VH} &= |S_{VH}|^2 + 2 \operatorname{Re} \{ S_{VH} (S_{VV} + S_{HH})^* \} \sin \gamma \cos \gamma \\ &\quad + (|S_{VV}|^2 + |S_{HH}|^2 + 2 \operatorname{Re} \{ S_{VV} S_{HH} \}) \sin^2 \gamma \cos^2 \gamma. \end{aligned} \quad (\text{B25})$$

If the expected value of  $\operatorname{Re} \{ \dots \}$  is 0 for surface scattering, then

$$P_{r,VH} = |S_{VH}|^2 + (|S_{VV}|^2 + |S_{HH}|^2) \sin^2 \gamma \cos^2 \gamma. \quad (\text{B26})$$



When  $\gamma$  is 0 (i.e., no pitch relative to the ocean surface and thus no polarization mixing),  $\sigma_{xy}^0 \propto P_{r,xy} = |S_{xy}|^2$ . Using this relationship to translate into NRCS instead of scattering coefficients, (B26) becomes

$$\sigma_{\text{VH}}^{\prime 0} = \sigma_{\text{VH}}^0 + (\sigma_{\text{VV}}^0 + \sigma_{\text{HH}}^0) \sin^2 \gamma \cos^2 \gamma \quad (\text{B27})$$

where the prime symbol indicates the measured quantity.

#### ACKNOWLEDGMENT

The authors would like to thank the NOAA/NESDIS Ocean Remote Sensing Program for its support of their flight experiment program; the NOAA Aircraft Operations Center (AOC) and the crew of N42RF for their assistance with this paper; the NOAA Hurricane Hunters for carrying out the repeated maneuvers that were required to obtain the data and for their patience, dedication, and diligence that provided a safe operating environment during data collection; the people at AOC, particularly Dr. J. McFadden, J. Roles, T. Lynch, J. Bosko, and W. Pullen, who made it possible for the ESA/RUAG antenna to be installed on the WP-3D aircraft before the Winter 2015 experiment; T. Hartley of the University of Massachusetts Amherst for helping in the installation and adaptation of the IWRAP system to the different antenna; M. Baker of NOAA/NESDIS/STAR for helping in keeping the data acquisition systems operating in the air during the experiment and providing support on the ground for the data processing; the European Space Agency, particularly C.-C. Lin and A. Østergaard; RUAG Space, particularly M. Petersson, P. Magnusson, and P. Dimming, for lending the antenna and providing technical assistance; and M. Ouellet of Fisheries and Oceans Canada for providing the buoy data and metadata, without which the NRCS data analysis would have been much more challenging.

#### REFERENCES

- [1] D. E. Fernandez, J. R. Carswell, S. Frasier, P. S. Chang, P. G. Black, and F. D. Marks, "Dual-polarized C- and Ku-band ocean backscatter response to hurricane-force winds," *J. Geophys. Res.*, vol. 111, no. C8, Aug. 2006, doi: 10.1029/2005JC003048.
- [2] P. W. Vachon and J. Wolfe, "C-band cross-polarization wind speed retrieval," *IEEE Geosci. Remote Sens. Lett.*, vol. 8, no. 3, pp. 456–459, 2011, doi: 10.1109/LGRS.2010.2085417.
- [3] B. Zhang, W. Perrie, and Y. He, "Wind speed retrieval from RADARSAT-2 quad-polarization images using a new polarization ratio model," *J. Geophys. Res.*, vol. 116, no. C8, Aug. 4, 2011, Art. no. C08008, doi: 10.1029/2010JC006522.
- [4] J. Horstmann, S. Falchetti, C. Wackerman, S. Maresca, M. J. Caruso, and H. C. Graber, "Tropical cyclone winds retrieved from C-band cross-polarized synthetic aperture radar," *IEEE Trans. Geosci. Remote Sens.*, vol. 53, no. 5, pp. 2887–2898, May 2015, doi: 10.1109/TGRS.2014.2366433.
- [5] G.-J. van Zadelhoff, A. Stoffelen, P. W. Vachon, J. Wolfe, J. Horstmann, and M. Belmonte Rivas, "Retrieving hurricane wind speeds using cross-polarization C-band measurements," *Atmos. Meas. Techn.*, vol. 7, no. 2, pp. 437–449, Feb. 7, 2014, doi: 10.5194/amt-7-437-2014.
- [6] F. Fois, P. Hoogeboom, F. Le Chevalier, and A. Stoffelen, "Future ocean scatterometry: On the use of cross-polar scattering to observe very high winds," *IEEE Trans. Geosci. Remote Sens.*, vol. 53, no. 9, pp. 5009–5020, Sep. 2015, doi: 10.1109/TGRS.2015.2416203.
- [7] D. E. Fernandez *et al.*, "IWRAP: The imaging wind and rain airborne profiler for remote sensing of the ocean and the atmospheric boundary layer within tropical cyclones," *IEEE Trans. Geosci. Remote Sens.*, vol. 43, no. 8, pp. 1775–1787, Aug. 2005, doi: 10.1109/TGRS.2005.851640.
- [8] C. Lin *et al.*, "Antenna development for MetOp second generation wind scatterometer," in *Proc. 9th EuCAP*, Lisbon, Portugal, Apr. 2015, 1–5.
- [9] P. Magnusson, P. Dimming, C. Lin, and A. Østergaard, "A thermally stable dual-polarized waveguide array," in *Proc. 9th EuCAP*, Lisbon, Portugal, Apr. 2015, 1–5.
- [10] R. J. Doviak and D. S. Zmíć, *Doppler Radar and Weather Observations*, 2nd ed. Mineola, NY, USA: Dover, May 26, 2006.
- [11] W.-C. Lee, P. Dodge, F. D. Marks, and P. H. Hildebrand, "Mapping of airborne doppler radar data," *J. Atmos. Ocean. Technol.*, vol. 11, no. 2, pp. 572–578, Apr. 1994.
- [12] S. Soisuvarn, Z. Jelenak, P. S. Chang, S. O. Alsweiss, and Q. Zhu, "CMOD5.H—A high wind geophysical model function for C-band vertically polarized satellite scatterometer measurements," *IEEE Trans. Geosci. Remote Sens.*, vol. 51, no. 6, pp. 1–17, Nov. 22, 2012, doi: 10.1109/TGRS.2012.2219871.
- [13] S. Soisuvarn, Z. Jelenak, P. S. Chang, Q. Zhu, and G. Sindic-Rancic, "Validation of NOAA's near real-time ASCAT ocean vector winds," in *Proc. IEEE IGARSS*, Boston, MA, USA, Jul. 7–11, 2008, vol. 1, pp. I-118–I-121, doi: 10.1109/IGARSS.2008.4778807.
- [14] D. B. Gilhouse, "A field evaluation of NDBC Moored Buoy winds," *J. Atmos. Ocean. Technol.*, vol. 4, no. 1, pp. 94–104, Mar. 1, 1987, doi: 10.1175/1520-0426(1987)004<0094:AFEONM>2.0.CO;2.
- [15] W. T. Liu, K. B. Katsaros, and J. A. Businger, "Bulk parameterization of air-sea exchanges of heat and water vapor including the molecular constraints at the interface," *J. Atmos. Sci.*, vol. 36, no. 9, pp. 1722–1735, Sep. 1, 1979, doi: 10.1175/1520-0469(1979)036<1722:BP0ASE>2.0.CO;2.
- [16] T. F. Hock and J. L. Franklin, "The NCAR GPS Dropwindsonde," *Bull. Amer. Meteorol. Soc.*, vol. 80, no. 3, pp. 407–420, Mar. 1999, doi: 10.1175/1520-0477(1999)080<0407:TNGD>2.0.CO;2.20.
- [17] E. W. Uhlhorn, P. G. Black, J. L. Franklin, M. Goodberlet, J. Carswell, and A. S. Goldstein, "Hurricane surface wind measurements from an operational stepped frequency microwave radiometer," *Month. Weather Rev.*, vol. 135, no. 9, pp. 3070–3085, 2007, doi: 10.1175/MWR3454.1.
- [18] J. L. Franklin, M. L. Black, and K. Valde, "GPS Dropwindsonde wind profiles in hurricanes and their operational implications," *Weather Forecast.*, vol. 18, no. 1, pp. 32–44, Feb. 1, 2003, doi: 10.1175/1520-0434(2003)018<0032:GDWPIH>2.0.CO;2.
- [19] B. W. Klotz and E. W. Uhlhorn, "Improved stepped frequency microwave radiometer tropical cyclone surface winds in heavy precipitation," *J. Atmos. Ocean. Technol.*, vol. 31, no. 11, pp. 2392–2408, Nov. 2014, doi: 10.1175/JTECH-D-14-00028.1.
- [20] J. Vogelzang, A. Stoffelen, A. Verhoef, and J. Figa-Saldaña, "On the quality of high-resolution scatterometer winds," *J. Geophys. Res.*, vol. 116, no. C10, Oct. 28, 2011, doi: 10.1029/2010JC006640.
- [21] A. Stoffelen, "Toward the true near-surface wind speed: Error modeling and calibration using triple collocation," *J. Geophys. Res.*, vol. 103, C4, 1998, Art. no. 7755, doi: 10.1029/97JC03180.
- [22] A. Verhoef, M. Portabella, A. Stoffelen, and H. Hersbach, "CMOD5.n—The CMOD5 GMF for neutral winds," *SAF/OSI/CBOP/KNMI/TEC/TN/165*, May 2008, (visited on Jun. 7, 2015), [Online]. Available: [http://www.knmi.nl/publications/fulltexts/cm05\\_neutral\\_winds\\_1.0.pdf](http://www.knmi.nl/publications/fulltexts/cm05_neutral_winds_1.0.pdf)
- [23] H. Hersbach, "CMOD5—An improved geophysical model function for ERS C-band scatterometry," ECMWF Techn. Memorandum 395, 2003, (visited on May 17, 2013), [Online]. Available: [http://www.ecmwf.int/publications/library/ecpublications/\\_pdf/tm/301-400/tm395.pdf](http://www.ecmwf.int/publications/library/ecpublications/_pdf/tm/301-400/tm395.pdf)
- [24] H. Hersbach, A. Stoffelen, and S. de Haan, "An improved C-band scatterometer ocean geophysical model function: CMOD5," *J. Geophys. Res.*, vol. 112, no. C3, Mar. 2007, Art. no. C03006, doi: 10.1029/2006JC003743.
- [25] A. Stoffelen and D. Anderson, "Scatterometer Data Interpretation: Measurement Space and Inversion," *J. Atmos. Ocean. Technol.*, vol. 14, no. 6, pp. 1298–1313, Dec. 1997, doi: 10.1175/1520-0426(1997)014<1298:SDIMS>2.0.CO;2.
- [26] P. A. Hwang, B. Zhang, J. V. Toporkov, and W. Perrie, "Comparison of composite Bragg theory and quad-polarization radar backscatter from RADARSAT-2: With applications to wave breaking and high wind retrieval," *J. Geophys. Res.*, vol. 115, no. C8, Aug. 19, 2010, doi: 10.1029/2009JC005995.
- [27] P. A. Hwang *et al.*, "Cross-polarization geophysical model function for C-band radar backscattering from the ocean surface and wind speed retrieval," *J. Geophys. Res.*, vol. 120, no. 2, pp. 893–909, Feb. 2015, doi: 10.1002/2014JC010439.
- [28] P. Hwang, W. Perrie, and B. Zhang, "Cross-polarization radar backscattering from the ocean surface and its dependence on wind velocity," *IEEE Geosci. Remote Sens. Lett.*, vol. 11, no. 12, pp. 2188–2192, Dec. 2014, doi: 10.1109/LGRS.2014.2324276.
- [29] A. Voronovich and V. Zavorotny, "Sensitivity of modeled polarimetric radar ocean scattering to wind direction," in *Proc. IEEE IGARSS*, Jul. 13–18, 2014, pp. 5021–5024, doi: 10.1109/IGARSS.2014.6947624.

- [30] B. Zhang *et al.*, "Ocean vector winds retrieval from C-band fully polarimetric SAR measurements," *IEEE Trans. Geosci. Remote Sens.*, vol. 50, no. 11, pp. 4252–4261, Nov. 2012, doi: 10.1109/TGRS.2012.2194157.
- [31] S. H. Yueh, S. J. Dinardo, A. G. Fore, and F. K. Li, "Passive and active L-band microwave observations and modeling of ocean surface winds," *IEEE Trans. Geosci. Remote Sens.*, vol. 48, no. 8, pp. 3087–3100, Aug. 2010, doi: 10.1109/TGRS.2010.2045002.
- [32] S. Yueh, W. Wilson, and S. Dinardo, "Polarimetric radar remote sensing of ocean surface wind," in *Proc. IEEE IGARSS*, Sydney, NSW, Australia, 2001, vol. 3, pp. 1557–1559, doi: 10.1109/IGARSS.2001.976909.



**Joseph W. Sapp** (S'04–M'06) received the B.S. degree in electrical engineering from the Pennsylvania State University, University Park, PA, USA in 2006 and the Ph.D. degree in electrical and computer engineering from the University of Massachusetts Amherst, Amherst, MA, USA, in 2015.

From 2006 to 2009, he was a Project Electrical Engineer with Lutron Electronics Company, Inc., Coopersburg, PA, USA, where he was involved in the embedded software design of multiple commercial products. In 2009, he joined the Microwave Remote Sensing Laboratory (MIRSL), University of Massachusetts Amherst, as a Research Assistant, where he first had the opportunity to participate in flight experiments with the NOAA Hurricane Hunters. Since 2015, he has been with NOAA/NESDIS Center for Satellite Applications Research (STAR) as a Support Scientist with Global Science & Technology, Inc., Greenbelt, MD, USA. His research interests include using active and passive microwave sensors to improve the algorithms and technology used in remote sensing of ocean surface wind vectors.



**Suleiman O. Alswess** (S'06–M'11) received the B.E. degree in electrical engineering from Princess Sumaya University for Technology, Amman, Jordan, in 2004 and the M.S. and Ph.D. degrees in electrical engineering from the University of Central Florida (UCF), Orlando, FL, USA, in 2007 and 2011, respectively.

From 2006 to 2011, he was a Research Assistant with the Central Florida Remote Sensing Laboratory, UCF, where his primary research focused on active and passive microwave remote sensing. In 2011, he joined the NOAA/NESDIS Center for Satellite Applications Research (STAR), College Park, MD, USA, as a Support Scientist with Global Science and Technology, Inc., Greenbelt, MD, USA, where he continues his work on calibrating, developing, and validating geophysical retrieval algorithms and products in an operational environment.



**Zorana Jelenak** (S'97–M'04) received the Ph.D. degree in physics from The University of Waikato, Hamilton, New Zealand, in 2000.

In March 2001, she joined the Ocean Winds Team at NOAA/NESDIS Office of Research and Applications as a UCAR Visiting Scientist. She is a member of the NASA Ocean Surface Winds Science Team, NOAA's EDR algorithm lead for AMSR-2 radiometer, and a member of the NASA CYGNSS Science Team. She is currently with the NOAA/NESDIS Center for Satellite Applications Research, College

Park, MD, USA. Her research interests include ocean surface wind vector measurements from active and passive microwave sensors and their applicability in an operational near-real time environment, retrieval algorithm development, model function development, advanced statistical analysis, and error analysis for improved algorithm characterization.



**Paul S. Chang** (S'87–M'90) received the B.S. degree in electrical engineering from Union College, Schenectady, NY, USA, in 1988 and the Ph.D. degree in electrical engineering from the University of Massachusetts Amherst, Amherst, MA, USA, in 1994.

Since 1994, he has been a Research Physical Scientist with the NOAA/NESDIS Center for Satellite Applications and Research, College Park, MD, USA. His current activities include research and development in active and passive microwave remote sensing of the ocean surface with emphasis on retrieval of the ocean surface wind field. Wind retrieval algorithm improvements and new product developments are pursued through the analyses of satellite and aircraft microwave remote sensing data. An emphasis is placed on transitioning research results into operational use, which involves cooperative relationships with the operational facets of NESDIS and with the National Weather Service, a primary end user of these data. Current efforts are focused on working on the METOP, RapidScat, CYGNSS and GCOM-W missions in addition to planning and risk reduction activities for future ocean vector winds missions.



**Stephen J. Frasier** (M'93–SM'05) received the B.E.E. degree from the University of Delaware, Newark, DE, USA, in 1987 and the Ph.D. degree from the University of Massachusetts Amherst, Amherst, MA, USA, in 1994.

From 1987 to 1990, he was with SciTec, Inc., Princeton, NJ, USA, analyzing the electromagnetic and optical signatures of rocket plumes, evaluating laser detection systems, and developing data acquisition systems supporting airborne IR sensors. In August 1990, he joined the Microwave Remote Sensing Laboratory, University of Massachusetts Amherst, where his graduate work involved the development and application of a digital-beamforming phased-array radar for oceanographic research applications. In 1997, he joined the faculty at the University of Massachusetts Amherst, where he is currently a Professor and Director of the Microwave Remote Sensing Laboratory. He currently leads radar research programs studying ocean surface winds and advanced radar methods for estimating winds in the atmospheric boundary layer. His research interests include microwave imaging and interferometric techniques, radar oceanography, and radar meteorology.

Dr. Frasier is a member of the IEEE Geoscience and Remote Sensing Society, URSI Commission F, the American Geophysical Union, and the American Meteorological Society.



**James Carswell** (S'88–M'95) received the B.S.E.E. degree from Tufts University, Medford, MA, USA in 1990 and the Ph.D. degree in electrical engineering from the University of Massachusetts Amherst, Amherst, MA, in 1995.

He is a Co-founder and the President of Remote Sensing Solutions, Inc. and an Adjunct Professor with the University of Massachusetts Amherst. As a co-founder and the President of Remote Sensing Solutions, he serves as a Principal Investigator and Technical Leader in providing radar systems, digital subsystems, and data management solutions for remote sensing applications. He was the initial Principal Investigator on the development of the Imaging Wind and Rain Airborne Profiler (IWRAP) and has led the development of the ARENA digital subsystem technology to further advance IWRAP's capabilities. He has developed several solid-state airborne and ground-based Doppler radars for atmospheric and oceanic research. As the Lead System Engineer, he designed and developed high-altitude, multichannel Ka-band interferometric radars for centimetric-level topography mapping. He is currently leading efforts to develop and deploy interferometric, digital beamforming millimeter-wave airborne radars, and ultrawideband millimeter-wave profiling radars for situational awareness, mapping, and security applications. He has worked in the area of microwave and millimeter-wave remote sensing since 1991.